

OF NEEDLES AND HAYSTACKS: SPATIALLY RESOLVED GAS KINEMATICS IN STARBURST GALAXIES HARO 11 AND ESO 338 FROM NUV/OPTICAL LONG-SLIT SPECTROSCOPY.¹

T. EMIL RIVERA-THORSEN^{2, 3}, GÖRAN ÖSTLIN^{2, 3}, ARJAN BIK^{2, 3}, MATTHEW HAYES^{2, 3}, AND ANDREAS SANDBERG^{2, 3}

¹Based on observations made with the ESO Telescopes at the Paranal Observatory under program 60.A-9433(A).

²Department of Astronomy, Oskar Klein Centre, Stockholm University, AlbaNova University Centre, SE-106 91 Stockholm, Sweden

³Oskar Klein Centre for Cosmoparticle Physics, Department of Astronomy, Stockholm University, Stockholm, Sweden

ABSTRACT

The ISM of starburst galaxies are well known to contain a wide variety of physical conditions and show complex kinematics. Still, when describing them spectroscopically, we often rely on one number to characterize each physical property, derived from data integrated over the entire slit. In this paper, we present a highly detailed spatial and kinematic decomposition of the spectra of three strongly star forming regions in nearby Lyman Break Analogs Haro 11 and ESO 338. The high-detail model we build allows to then investigate the variety of physical conditions present in the warm gas in various location along the slit and along the line of sight, using kinematics and extinction as markers of depth. We perform a number of commonly used line ratio based diagnostics on individual subsystems, allowing us to give an unprecedentedly detailed description of the overall kinematic and physical properties of the systems, while also seeking out subsystems and regions with peculiar behavior. We identify ionized bubbles, large scale outflows and use the kinematic decomposition to get a view into the spatially unresolved hot and bright central regions. We find signs of local rotation around knot B in Haro 11, while the other targets seem to display no ordered motion. We present circumstantial evidence that knot B in Haro 11 may host an accreting intermediate to high mass black hole, and discuss other components of particular interest.

1. INTRODUCTION

Starburst galaxies are galaxies undergoing intense star formation, rapidly consuming their reservoirs of neutral hydrogen (see e.g. Kennicutt 1998). They are not a well defined class of objects (see e.g. Bergvall et al. 2016, and references herein), as a starburst episode can be either global or local and can take place in a wide range of galaxy types. Starburst episodes are usually triggered by strong gas interactions, either by infalling intergalactic or circumgalactic medium (IGM/CGM) or, more commonly at low redshifts, by galaxy-galaxy interactions or mergers (Combes 2005; Overzier et al. 2008, 2009). Mergers of massive, late-type galaxies tend to be develop into dusty starbursts of the (Ultra-) Luminous Infrared Galaxies ((U)LIRGs, Bergvall et al. 2016, and references herein), while lower mass galaxies will have less dust and are characterized by strong blue/UV colors; such starbursts show as Blue Compact Galaxies (BCGs), Blue Compact Dwarfs (BCDs), or Green Pea-type galaxies (Cardamone et al. 2009). Local and low-redshift starbursts of the low-mass, dust poor type have been shown to be useful as Lyman Break Analogs (LBAs, see e.g. Heckman et al. 2005; Hoopes et al. 2007), or as analogs of high-redshift Lyman Alpha Emitters

(LAE, see e.g. Östlin et al. 2014; Hayes et al. 2014) for a discussion), and for studying the effect of feedback on large scales. Starburst galaxies are, in short, valuable local laboratories for the detailed study of galaxy evolution and conditions in the early Universe.

Starbursts have complex ISM dynamics. For one, the ISM is strongly modified by feedback from star formation, and are surrounded by large ionized halos (Östlin et al. 1999, 2001; Bergvall & Östlin 2002; Cumming et al. 2008; Bik et al. 2015; Östlin et al. 2015). When studying them spectroscopically, we often rely on one single number to quantify a given property, obtained from a spectrum integrated over the entire slit or aperture of the spectrograph. However, to fully catch the complexity and variety of physical conditions that can be found in the ISM of a starburst galaxy, spatially resolved spectroscopy is required. Some work has been done in this regard, either with Integral Field Units (e.g. Sandberg et al. 2013; James et al. 2013; Östlin et al. 2015; Bik et al. 2015; Herenz et al. 2016) or with spatially resolved long-slit spectroscopy (Östlin et al. 2015).

In this work, present a novel method for modeling nebular emission in high spatial and kinematic resolution from 2D long-slit spectra of high signal-to-noise ratio

(SNR). Combined with the good spectral resolution and very high wavelength coverage range of the X-Shooter spectrograph at the Very Large Telescope (Vernet et al. 2011), we achieve a highly detailed model of a number of Balmer and forbidden metal emission lines, which we use to identify a number of subsystems in our targets which can then be individually analyzed with commonly used line ratio-based diagnostics. The amount of information available in these spectra and models is large, and we have far from exhausted the possibilities.

1.1. Sample

We focus our attention on the two well-studied, nearby starbursts ESO 338-IG04 (in the remainder of this work, ESO 338), also known under the name of Tololo 1924-416, and Haro 11, also known as ESO 350-IG38. Haro 11 is a strong starburst at redshift $z \approx 0.021$. It is a strong starburst producing stars at a rate of $\sim 22 \pm 3 M_{\odot}/\text{yr}$ (Adamo et al. 2010), with an older, underlying population (Adamo et al. 2010; Micheva et al. 2010). The central starburst region is concentrated in three main star-forming knots, first denoted A, B and C by the terminology of Vader et al. (1993); Kunth et al. (2003), see fig. 1. It is seen as a Lyman Break Analog (Hoopes et al. 2007). It is strong Lyman α emitter (Kunth et al. 2003) and a LAE analog (Hayes et al. 2007; Leitert et al. 2011), although the Ly α radiation is strongly inhomogeneous, with knot C being a strong emitter and knot B being a strong absorber (Hayes et al. 2007). It is one of very few known local galaxies to leak Lyman Continuum (Leitert et al. 2011). It has been found to have strongly unordered internal motion (Östlin et al. 1999, 2001, 2015) and is chemically strongly inhomogeneous (James et al. 2013). Östlin et al. (2015) present compelling evidence that Haro 11 currently undergoing a merger process, pointing out numerous similarities to the nearby, and larger, Antennae galaxy.

ESO 338 is, like Haro 11, strongly star forming and its ISM strongly affected by feedback. The galaxy has a smaller companion galaxy which probably has been stripped of much of its gas in an interaction (Östlin et al. 1998; Bergvall & Östlin 2002; Cannon et al. 2004); it is unclear whether this companion galaxy will escape or they will eventually merge. The starburst is likely to have been triggered by a merger, either with a dwarf galaxy or a large gas cloud, but is too young to have been triggered by the latest passage of the companion (Cumming et al. 2008). The central part, which is treated here, is dominated by a super star cluster with a mass as large as $\sim 10^7 M_{\odot}$ (Östlin et al. 2007), which has completely ionized a surrounding bubble. Also this target shows complex ISM kinematics (e.g. Hayes et al. 2005; Cumming et al. 2008; Bik et al. 2015).

The spectra analyzed in this work were obtained as

part of the ESO X-Shooter science verification campaign and have been publicly available since. They have so far been analyzed and described by Sandberg et al. (2013) and Guseva et al. (2012).

The remainder of this paper is structured as follows: In sect. 2, we present the observations, reduction, rectification and other similar steps. In sect. 3, we describe the method for building the model, fit quality indication, and uncertainty estimates. The impact of stellar Balmer absorption is discussed. Section 4 presents the models and parameters derived from line ratios for each component. In sect. 5, we discuss the physical implications of our findings, and finally sect. 6 gives a summary and conclusion.

2. OBSERVATIONS AND DATA REDUCTION

2.1. Observations

The spectra treated in this work were obtained as part of the science verification program of the ESO X-Shooter (Vernet et al. 2011), under program ID 60.A-9433(A) PI Östlin, on August 11th and 12th, 2009. The X-Shooter is an intermediate-resolution, high-range echelle spectrograph sensitive to a wavelength range of $\sim 3000 \text{ \AA}$ to $\sim 2.5\mu$, in three arms covering the wavelength ranges $\sim 3000 - 5600 \text{ \AA}$ (UVB), $\sim 5500 - 10200 \text{ \AA}$ (VIS), and $\sim 1.0 - 2.5\mu$ (NIR), each arm having its own slit and set of optics, optimized for their respective wavelength ranges. The observations were made at an airmass / seeing of 1.458 / 0.59-0.66, 1.014 / 0.73-1.32, 1.012 / 0.7-0.71 for ESO 338, Haro 11 B and Haro 11 C, respectively, with the Atmospheric Dispersion Correction (ADC) unit enabled. For these observations, a slit of $0.9 \times 11''$ for the VIS and NIR arms, and $0.8 \times 11''$ for the UVB arm. The UVB and NIR arms have a resolution of $R = 5100$, the VIS arm $R = 8800$. The observations were performed in “nodding” mode, in which two exposures of equal length are made with the target offset by $4''$ between the exposures, at combined exposure times of 600 s (ESO 338), 800 s (Haro 11 B) and 680 s (Haro 11 C).

Figure 1 shows the approximate pointing and rotation of the slits, and the combined extent of the two nodding positions, with a synthesized slit length of $14.4''$. The knots in Haro 11 are labelled according to the scheme of (Vader et al. 1993; Kunth et al. 2003), the two spectra are centered on knots B and C. In ESO 338, the slit is centered on cluster # 23 in the inner sample of (Östlin et al. 1998), henceforth simply cluster 23. Both frames are oriented so North is up, East is left; background images are made with image from (Hayes et al. 2009; Östlin et al. 2009).

2.2. Reduction

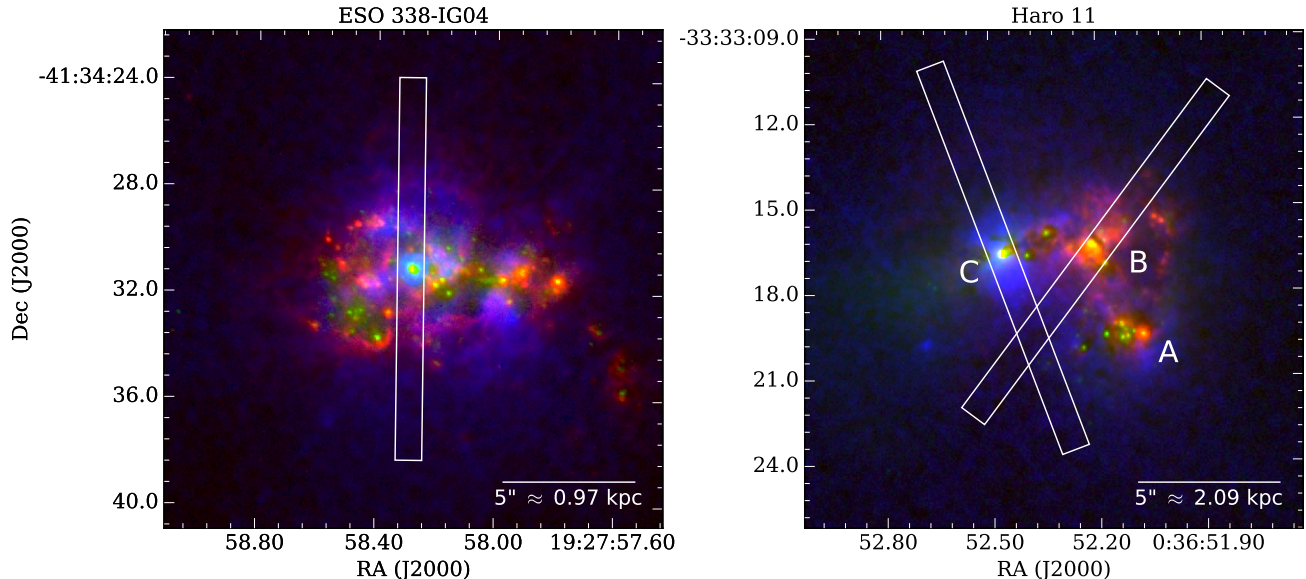


Figure 1. Approximate coverage of the synthesized $14.4''$ slit overlaid on false-color images of Haro 11 and ESO 338. Red in the images represents continuum subtracted $H\alpha$; blue represents continuum subtracted Lyman α , and green represents UV continuum. Colors are log-scaled and cut levels set to enhance detail. Image composite made with data from (Hayes et al. 2009; Östlin et al. 2009). The star forming knots of Haro 11 are labelled as introduced in (Kunth et al. 2003); both frames are aligned so N is up and E is left.

The spectra were reduced using v. 2.6.8 of the X-Shooter reduction pipeline provided by ESO, using v. 3.12 of the `esorex` interface. The pipeline was run in the recommended `physmod` mode using standard settings except that instead of the standard science reduction step for the `nodding` mode, the final science reduction step was performed with the recipe `xsh_scired_slit_stare`, leaving sky emission unsubtracted and continuum trace off center. The spectrum pairs, with a slit length of $11''$ each, were then offset by the `NOD THROW` given in the FITS header, and combined into one 2D spectrum representing a synthetic slit length of $14.5''$ at a spatial pixel scale of $0.16''$. The spectra were flux calibrated using the flux standard star LTT 7987; no telluric standard star was observed as part of the program, so telluric absorption lines have been left uncorrected. This means we have not been able to include the $[S II] \lambda\lambda 6717, 35$ in the two spectra of Haro 11.

The reduced, flux calibrated and extracted 1D spectra are shown in Fig. 2. The spectra have been truncated at rest frame $\lambda = 7500 \text{ \AA}$, a range comfortably covering the lines analyzed in this work and giving a good idea of the continuum shape, while still allowing for single lines to remain visible in some detail.

2.3. Continuum trace

In the 2D products of the reduction pipeline, the continuum trace is not well aligned in the center of the slit; a problem particularly conspicuous in the 2D spectra of

the VIS arm. We have not been able to determine the cause of this.

Since our analysis depends strongly on a 1:1 correspondence between pixel coordinate along the slit and actual spatial position, we performed a rectification procedure on the 2D spectra, fixing the continuum trace at its value at $H\alpha$ line center. The procedure of this is described in further detail in appendix A.

Figures 3, 4, and 5 show cutouts of the 2D spectrum around the most important lines treated here after continuum alignment has been performed. It is clear from quick inspection that the lines show a wealth of complex kinematic features, of which the most dramatic is probably the ring structure immediately above the continuum trace in Haro 11 B, which we shall discuss later.

2.4. Separating $H\alpha$ and $[N II]$

In the two observed regions of Haro 11, the line feature of $H\alpha$ is broad enough to blend with the neighbouring lines of $[N II] \lambda\lambda 6548, 6583$. In order to remove this contamination, we utilized the fact that the two $[N II]$ transitions have a fixed line ratio $A_{6583}/A_{6548} = 2.9573$ (Kramida et al. 2013), that the surrounding continuum is close to constant, and assumed that contamination by one line in a second line is negligible on the far side of the latter. From this, we computed the $[N II]$ -subtracted $H\alpha$ feature, and two $H\alpha$ subtracted $[N II]$ lines, in the following way:

First, the surrounding continuum was modelled and subtracted. Despite the small wavelength separation

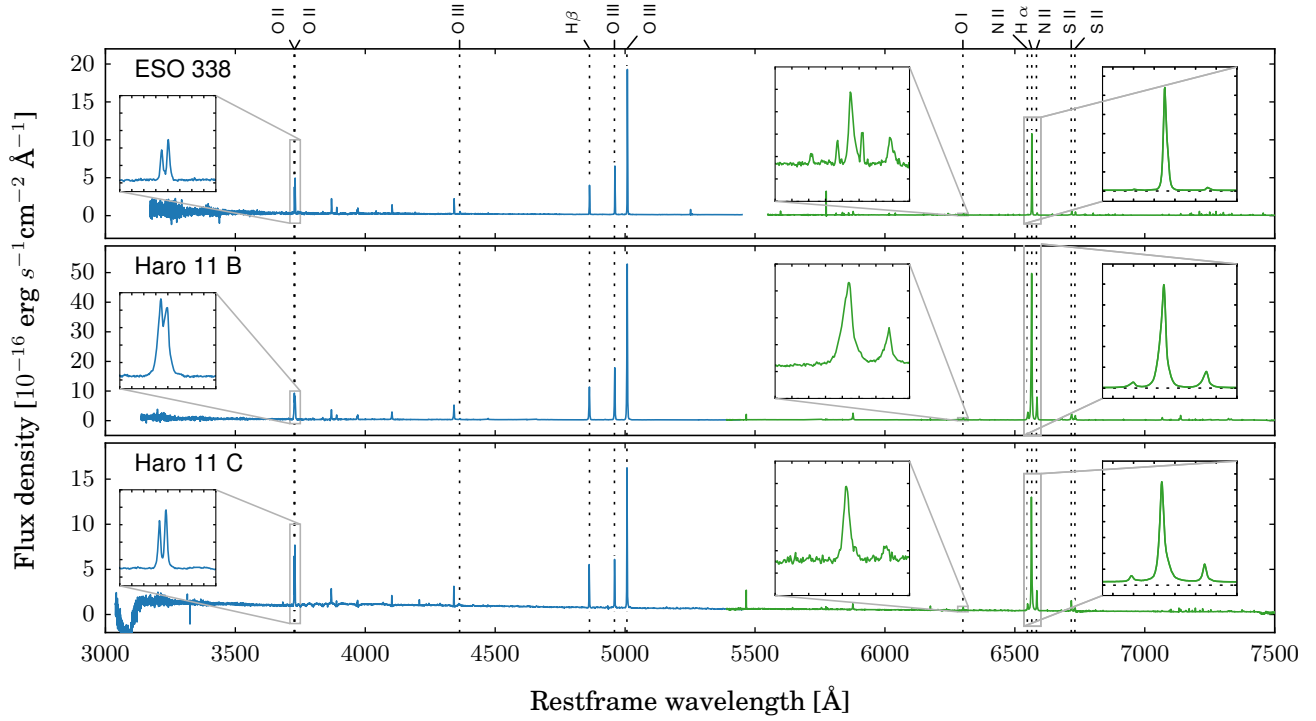


Figure 2. The flux calibrated spectra, extracted to show continuum shape and relative strengths of the strongest lines. Inset on the left is for each spectrum the zoomed-in line of [O II] 3726, 29; inset to the right shows a zoom on H α and the surrounding [N II] doublet. The data of the VIS arm is shown in green, of the UVB arm in blue.

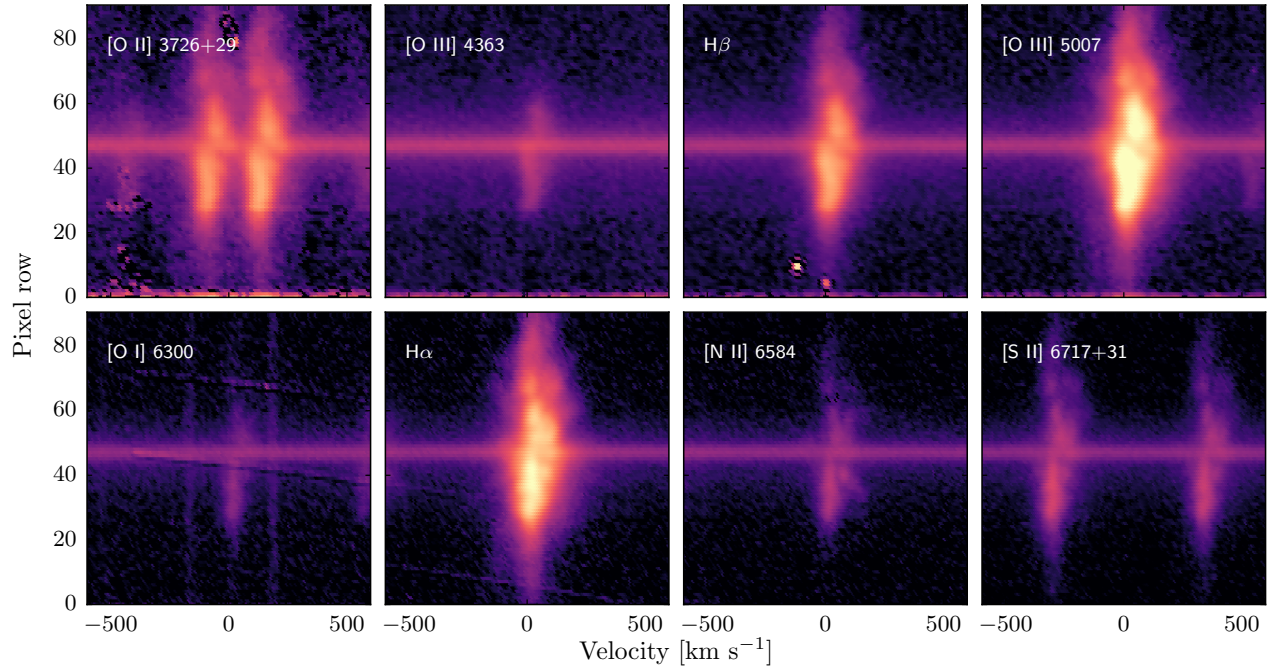


Figure 3. Cutouts from the 2D spectrum of ESO 338 of the lines analyzed in this work. Doublets are shown on a velocity scale relative to the mid point of their line centers. Colors are scaled logarithmically and cut levels set to enhance detail.

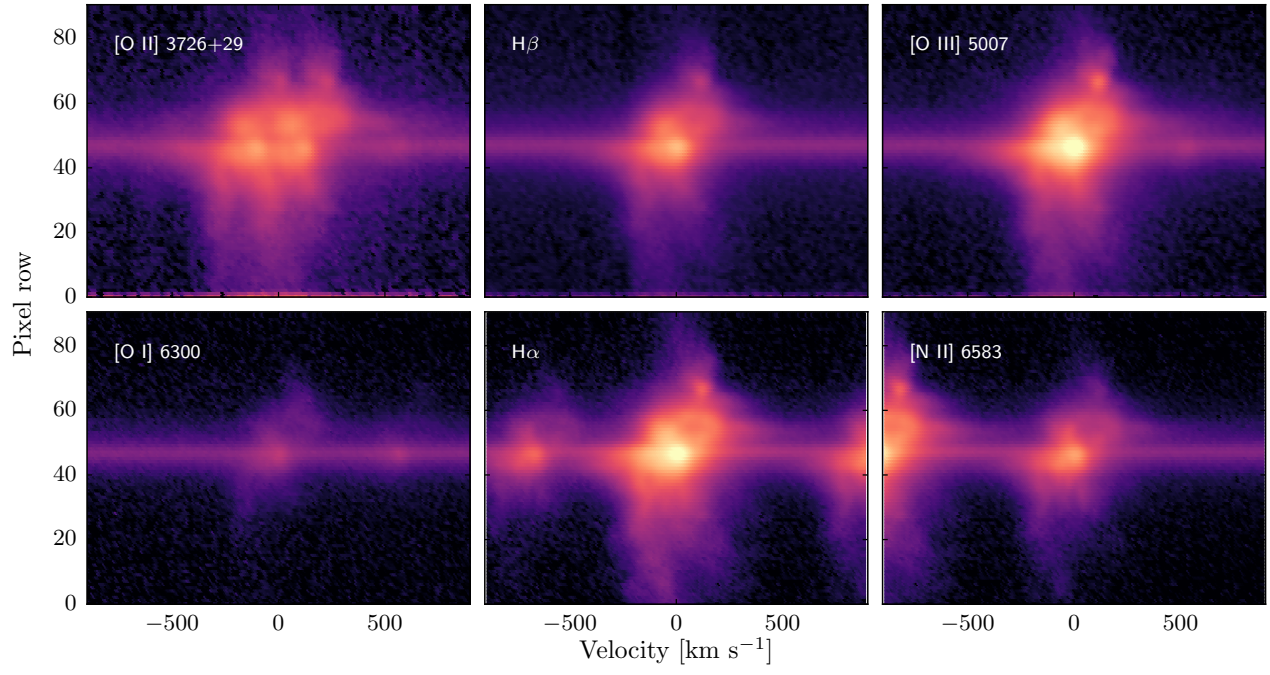


Figure 4. Same as fig. 3, but for Haro 11 B.

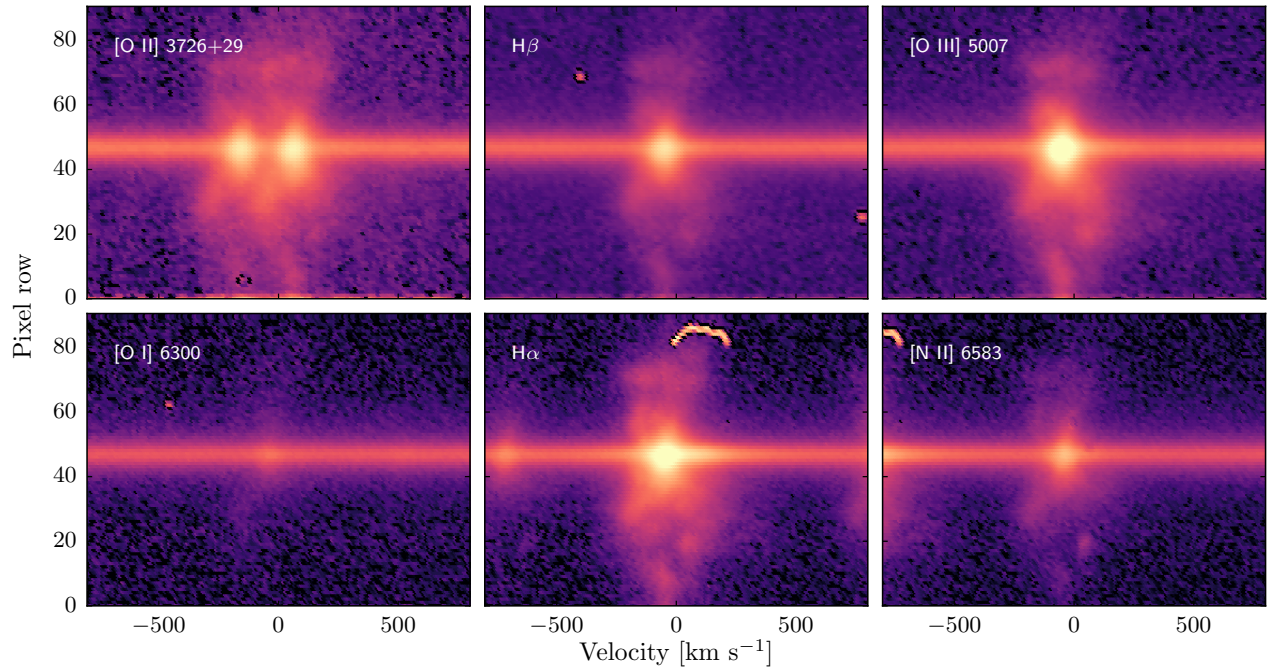


Figure 5. Same as fig. 3, but for Haro 11 C.

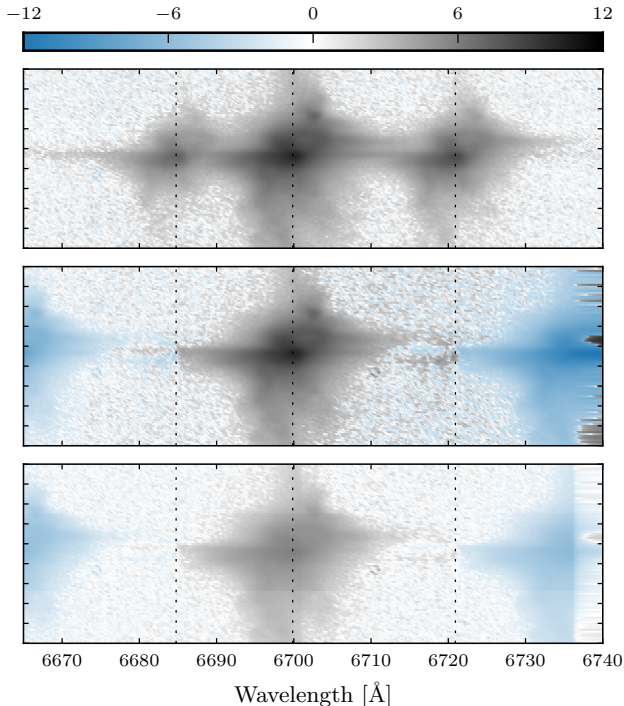


Figure 6. **Upper panel:** Continuum-subtracted H α and [N II] profiles of Haro 11 B. **Middle panel:** Same, with interpolated and scaled [N II] profiles subtracted. **Lower panel:** [N II]-subtracted spectrum in terms of error spectrum shows that the residual features from the neighboring [N II] λ 6583 feature are of $\lesssim 1\sigma$. Dotted vertical lines mark the systemic center of each line. Colors are asinh-scaled, and cut levels set to show maximum detail.

two [N II] lines, the wavelength-to-velocity conversion is slightly different. Therefore, each of the two features had to be interpolated onto the velocity grid of the other, again using the `ErrorPropagationSpline` class, and scaled by the line ratio to match its line strength with the other. Assuming that the contribution of H α on the red side of [N II] λ 6583 is negligible, the scaled and interpolated red side of this transition could then be taken to represent the true, uncontaminated [N II] λ 6548 feature and thus, when subtracted from the original data, left behind a reconstruction of the true and unblended blue wing of H α . This procedure was repeated by subtracting the scaled, interpolated blue side of the λ 6548 feature from the other, reconstructing the red wing of H α . This cleaned H α profile could then be subtracted from the original spectrum to remove H α contamination from the [N II] lines.

The result is shown for Haro 11 B in figure 6. The upper panel shows the triplet with continuum subtracted to avoid visually drowning out residuals in the central region; continuum is not subtracted in the version on which we built our model. The middle panel shows H α with the interpolated and scaled [N II] profiles subtracted. The red side of the [N II] features suggests that

there is in fact a weak H α contamination in the spatially central region of [N II] λ 6548, which leads to a slight over-subtraction in [N II] λ 6583. However, the lower panel shows that in terms of the error spectrum, this effect is weak.

2.5. Effective resolution estimation

In order to estimate the width of the instrument line spread function (LSF), we noted that the majority of the emission we model is extended, nebular emission, the resolution of which is limited by the slit width. The width of sky emission lines can therefore serve as an estimator of the instrument profile for our purpose. We selected a number of sky emission lines from the UVES Sky Atlas (Hanuschik 2003) which appear sufficiently isolated to not risk being blended and thus skew the width estimate. Each line was then fitted to a single Gaussian profile, to investigate how their width depend on wavelength. We found that assuming the width to be constant in velocity space was a good approximation to the measured width, and this was adopted. In the case of the UVB arm, only four sky lines were present living up to the selection criteria, three of which were too faint to be reliably fitted. However, it was still found that the observations were well modelled by assuming the LSF to be constant in velocity.

3. MODELING

3.1. Stellar absorption in Balmer lines

3.1.1. Impact on nebular emission

To assess the impact of stellar absorption on the measured fluxes, we fitted the Balmer lines H β through δ for each target. This was only carried out for central regions, as the exposures were too shallow to probe the stellar continuum at low luminosities, far from the central clusters. Emission line models were simplified to two Gaussian components, just enough to get a reasonable modelling of the line, and the absorption feature as one single Gaussian profile. The width of the absorption Gaussian was given a lower limit well broader than the emission feature, as it would otherwise easily become a fudge factor in the modeling of emission. A maximum FWHM of 25 \AA was set. Especially in Haro 11 B, where the emission feature is very broad, the setting of a minimum width has not been efficient everywhere, and a few places the absorption feature does indeed seem to have gotten unreasonably deep, improving the fit of the emission feature rather than modelling the actual absorption feature. However, such cases will tend to also have large uncertainties and thus not affect any weighted quantities strongly. We have therefore controlled that none of these cases were present in the section of data in Haro 11 C which was compensated for underlying absorption, but otherwise left them as they were.

After modelling the stellar absorption feature, we measured the flux in $H\beta$ emission with and without compensating for underlying stellar absorption. Uncertainties were estimated by Monte Carlo sampling. Differences between absorption-corrected and uncorrected flux are presented for the lines in the central clusters in table 1, along with the measured Equivalent Widths $EW_{abs}(H\beta)$. The stellar population is expected to be older and the stellar absorption accordingly stronger away from the central source, but stellar continuum is so much fainter there that the impact on the nebular emission is weak off-center. Only in Haro 11 C does the difference between corrected and uncorrected line emission flux exceed 1%, getting as high as $\sim 7\%$ in the central region. This has a modest effect on the integrated flux in $H\beta$. However, faint but broad components could be strongly underestimated in $H\beta$, leading to corresponding overestimates of dust reddening and other derived properties involving the flux in $H\beta$ for such components. We therefore subtracted the modelled absorption feature from the central half of the rows of Haro 11 C in $H\beta$. No other corrections for stellar absorptions have been done as it would only introduce systematic uncertainties while changing little in the data.

3.1.2. Age of stellar population

From absorption EWs, we inferred the age of the stellar population from table 5 in González Delgado et al. (1999), assuming a single instantaneous burst and a metallicity of $Z = 0.001$ - a very good approximation for the metallicity of ESO 338. Because we are fitting a Gaussian from its wings alone, the measured EWs and inferred stellar ages can in some places be quite uncertain.

Stellar ages are shown in figure 7, with dashed, solid and dotted black lines showing ages inferred from EW in $H\beta$, $H\gamma$ and $H\delta$, respectively. While the inferred ages agree quite well in the central cluster, the poor S/N in the surrounding regions means that inferred ages can differ by as much as two orders of magnitude. The figure also shows a simple mean of the inferred ages (orange), and a mean weighted by the inverse variances of the equivalent widths (green). This weighting can change the inferred age quite dramatically, especially visible in the age profiles for ESO 338. Finally, the figures show in blue a *loess*-smoothed weighted-age profile (LOESS is a robust smoothing procedure described in more detail in section 3.3.2). From this profile, more robust to outliers than simple means, we have computed total ages for the rows 42-52 (the *Central* age), rows 30-40 (the *southern* age), and rows 55-65 (the *northern* age), by computing the average-of-averages in each group of rows, weighted by the continuum strength in each row. These ages agree fairly well with other estimates in the

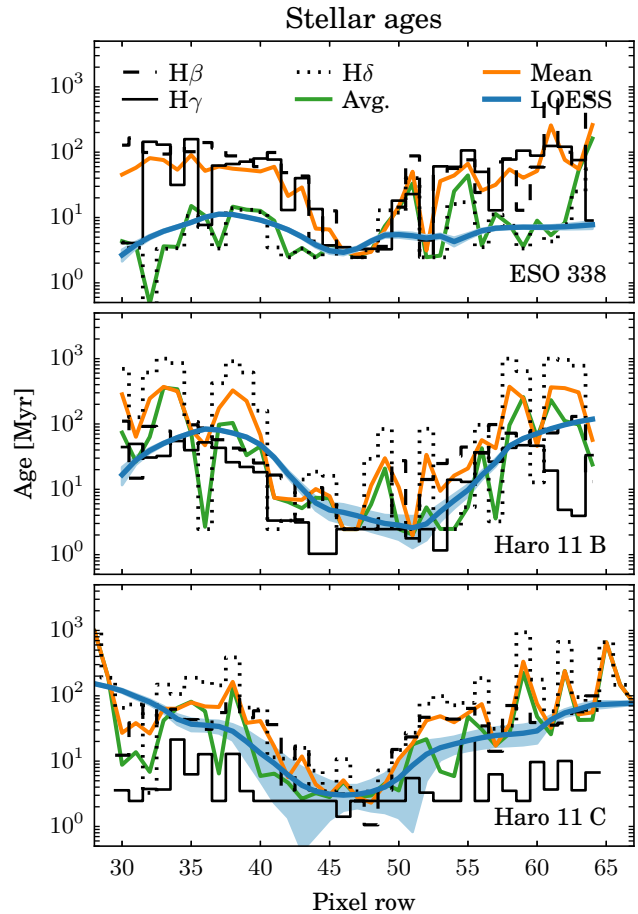


Figure 7. Inferred ages of the stellar population for each pixel row. **Black** solid, dashed and dotted steps show ages inferred from each individual transition. **Orange** lines show a simple mean of the three for each row. **Green** lines show an average weighted by the inverse variances, and **Blue** shows the LOESS-smoothed ages, also weighted by inverse variances, with light blue spanning the $\pm 1\sigma$ truncated confidence intervals.

literature for the central knots, for which the individual ages are also fairly consistent. The ages in the wings are more uncertain, and the width of the confidence intervals may be underestimated. The computed ages are summarized in table 7

Table 2. Stellar population age

| Age [Myr] | ESO 338 | Haro 11 B | Haro 11 C |
|-----------|---------------|----------------|----------------|
| (1) | (2) | (3) | (4) |
| Northern | 6.8 ± 0.1 | 48.8 ± 1.0 | 33.1 ± 2.6 |
| Central | 3.7 ± 0.1 | 3.7 ± 0.4 | 3.3 ± 0.7 |
| Southern | 8.4 ± 0.1 | 47.5 ± 0.8 | 41.9 ± 2.5 |

Table 2 continued

Table 1. Stellar absorption in central rows

| Row | ESO 338 | | Haro 11 B | | Haro 11 C | |
|-----|-------------------|---------------------|-------------------|-----------------------|-------------------|---------------------|
| | EW_{abs} | $\Delta F_{H\beta}$ | EW_{abs} | $\Delta F_{H\beta}$ | EW_{abs} | $\Delta F_{H\beta}$ |
| 44 | 4.6 ± 10.8 | 0.08% | 3.8 ± 8.6 | 1.3×10^{-10} | 3.0 ± 3.5 | 3.5% |
| 45 | 3.9 ± 10.0 | 0.35% | 3.1 ± 8.4 | 1.2×10^{-5} | 2.8 ± 3.1 | 4.7% |
| 46 | 1.5 ± 9.8 | 0.40% | 1.8 ± 6.7 | 1.5×10^{-4} | 2.5 ± 1.9 | 5.6% |
| 47 | 0.8 ± 2.2 | 0.44% | 2.2 ± 7.4 | 1.8×10^{-7} | 2.3 ± 1.8 | 5.6% |
| 48 | 1.8 ± 6.0 | 0.27% | 0.7 ± 3.9 | 1.2×10^{-10} | 2.4 ± 1.5 | 6.1% |
| 49 | 3.5 ± 9.6 | 0.28% | 3.2 ± 8.2 | 4.8×10^{-12} | 3.2 ± 2.8 | 6.7% |
| 50 | 5.2 ± 10.2 | 0.20% | 6.4 ± 10.3 | 5.4×10^{-6} | 4.4 ± 5.4 | 6.6% |

Table 2 (*continued*)

| Age [Myr] | ESO 338 | Haro 11 B | Haro 11 C |
|-----------|---------|-----------|-----------|
| (1) | (2) | (3) | (4) |

NOTE—Uncertainty estimates are the propagated confidence intervals of the continuum-weighted ‘loess’ fitting of the error-weighted average absorption EWs, shown as light blue bands in fig. 7.

3.2. Kinematic decomposition of line emission

The kinematic model of each galaxy was initially built using $H\alpha$ as a template, reasoning that the neutral Hydrogen transitions would best trace the gas in the entire regions analyzed. The model was then copied to the other transitions and fitted with freely varying amplitude and fixed or tightly constrained line width and velocity, these constraints are described further below. Components that behave consistently and coherently over a range of rows in all three fitting parameters A , v and σ , were interpreted as originating in the same physical subsystem, which was assigned a single-letter label, through which it can later be paired with flux originating from the same physical subsystem in other transitions.

For a single, extracted spectrum, the established way to model multiple kinematic components would be to add a number of components and let the minimization algorithm settle on the combination that best models the data. The number of components included would typically be the number, beyond which the reduced χ^2 no longer improves. However, in this case we have the additional constraint that any single extracted spectrum should be modelled in a way consistent with that of adjacent regions. While kinematic components in the dispersion direction are well described by multiple combined Gaussians, there is no general functional form for how

the flux density of a region varies spatially, and thus we have not attempted modelling the systems in two dimensions. Instead, we initially modelled each row independently, largely leaving the choice of best fit to the minimization algorithm. We then looked for tendencies occurring in A , v , σ simultaneously, and lines discontinuously departing from these tendencies were re-modelled by providing the minimizer an initial guess close to the values of the adjacent rows and then attempting to have it settle on a model consistent with these.

3.2.1. Discontinuities

One difficulty in this approach is that spatial discontinuities can occur for several reasons, e.g. when the flux of one component dips below some critical value which causes the χ^2 to suddenly be better minimized by a different set of values in the remaining components. This can be seen especially clearly in Haro 11 B, where a dust lane right above the central source causes jumps in the configurations of some components.

3.2.2. Choice of number of components

The number of kinematic components to include in the model for each row was determined by the ability to reach consistency across adjacent rows. When overfitting a line, superfluous components generally will start fitting the noise in said line. When working with one integrated spectrum, it can be difficult to tell components apart that trace real physical features and noise. However, while real physical features are coherent at least down to the seeing, noise features are not. Thus, when working with the detector rows individually, noise-fitting components stand out rather conspicuously with a large, random variation in the fitting parameters, and can be weeded out relatively easily. Our approach has therefore been to deliberately add kinematic components until they started displaying this random behavior, after which these were removed and the rest kept. One should bear in mind that this approach does introduce a certain

bias, as this allows us to follow significantly fainter components in the fainter outskirts of the nebular regions; components of very low flux have been possible to trace in the end regions of the slit, while components of significantly higher flux may have been left unaccounted for in the central regions, being drowned out by the much stronger central components and their correspondingly higher noise levels.

3.2.3. Other transitions

Once the full range of rows were satisfactorily modelled, the model of $H\alpha$ was copied to the other transitions of interest, which were in this way assumed to have the same physical structure as $H\alpha$ and were fitted allowing only the amplitude of the components to vary freely. For other transitions in the VIS arm - [N II] 6583 and, in the case of ESO 338, the [S II] doublet at 6717+31, could be modelled well by simply fixing velocities and widths to the same values as for $H\alpha$, correcting for differences in the fitted LSF.

3.2.4. Morphological difference in UVB and VIS

Lines in the UVB arm, in particular [O III] 5007, were initially not as well fitted by this approach as lines in the VIS arm. Firstly, the narrower slit tells us that the LSF in the UVB arm must be different than that in the VIS arm, but due to the lack of strong sky emission lines in the UVB, we were not able to determine the LSF reliably. The corrective factor to the line widths - assuming that the LSF is a Gaussian - was therefore left as a degree of freedom when fitting [O III] λ 5007, by allowing the line widths to co-vary by a multiplicative factor of at most 0.1.

The problem of the poor fit however persisted in some regions of all three spectra even after correction of line widths. We speculated that O III traces slightly different physical regions than the Balmer lines, and thus we would expect to find a slightly different velocity structure here. However, it turned out that $H\beta$, tracing the very same atoms as $H\alpha$, morphologically shows better similarity with [O III], suggesting that this is an instrumental effect rather than something intrinsic to the targets. We believe that at least two effects play in:

Firstly, the VIS slit covers an area around 13% larger than the UVB slit, and thus traces regions slightly different from those in UVB. We believe that this is the most important effect. Secondly, sampling is coarser in the UVB, making it more sensitive to noise and, especially, to slight imprecisions in wavelength calibration between the two arms. This sensitivity will be strongest for bright, narrow lines, consistent with the fact that the discrepancy in fit quality was stronger for ESO 338.

When fitting [O III] 5007, the strongest line in the UVB, we therefore allowed the component velocities to

vary within $\pm 10 \text{ km s}^{-1}$, or slightly less than one pixel's width at the observed wavelength, while being allowed to co-vary in line width as described above. This in combination assures preservation of the overall kinematic structure of the line profile, while allowing for some wiggle to compensate for the slight differences in morphology. The modified centroid velocities and line widths of [O III] 5007 were then copied to the remaining transitions in the UVB arm, in the same manner the fixed widths and velocities of $H\alpha$ were given for the optical transitions. The easing of centroid velocity position constraints was not necessary to get a good fit for Haro 11 B. This target has the broadest lines of the three, further strengthening the case for sampling effects being at least part responsible for the dissimilarities.

Figure 8 shows an example model for each of the targets, in $H\alpha$, [O III] 5007, and in [O II] 3726+29; each for the pixel row of strongest $H\alpha$ flux. Observed data are shown as black steps, the composite model in orange, and the individual components as single Gaussians under the model, colored according to their label. Residuals are shown to scale above the models in gray color, around a zero-level marked by a gray horizontal line. For ESO 338 and Haro 11 C, the centroid velocities have been allowed to vary slightly between $H\alpha$ and [O III] λ 5007, but as is clear from inspection, the structure and decomposition of the line is largely unchanged.

Figure 9 gives an overview of the kinematic components of the models in $H\alpha$. Left panels show $H\alpha$ for comparison. Middle panels show the same with centroids of all components in all rows superimposed, colored according to their labels. Rightmost panels show flux-weighted averaged slit positions and velocities for the assumed physical subsystems. Here, marker areas encodes the mean flux density of the components, while their average line width σ is marked by the error bars. The averaged positions generally correspond well to bright clumps in the line image, although a long tail of low flux may pull the weighted centroid away from the visually brightest point. To enhance detail, colors for the transition images are scaled logarithmically; the subsystem fluxes are better reflected in the marker areas. Flux-weighted slit positions of components reported here are later adopted as spatial positions of the subsystems.

3.3. Fit quality indication and uncertainty estimates

3.3.1. Residuals

The line shapes and kinematic structures of our targets are rich and complex, and the SNR high. For a given spectrum, it would be possible with good confidence to build a model of more components than has been done in this work. However, the added requirement of model consistency between adjacent rows renders this unfeasible; as described in section 3.2, adding

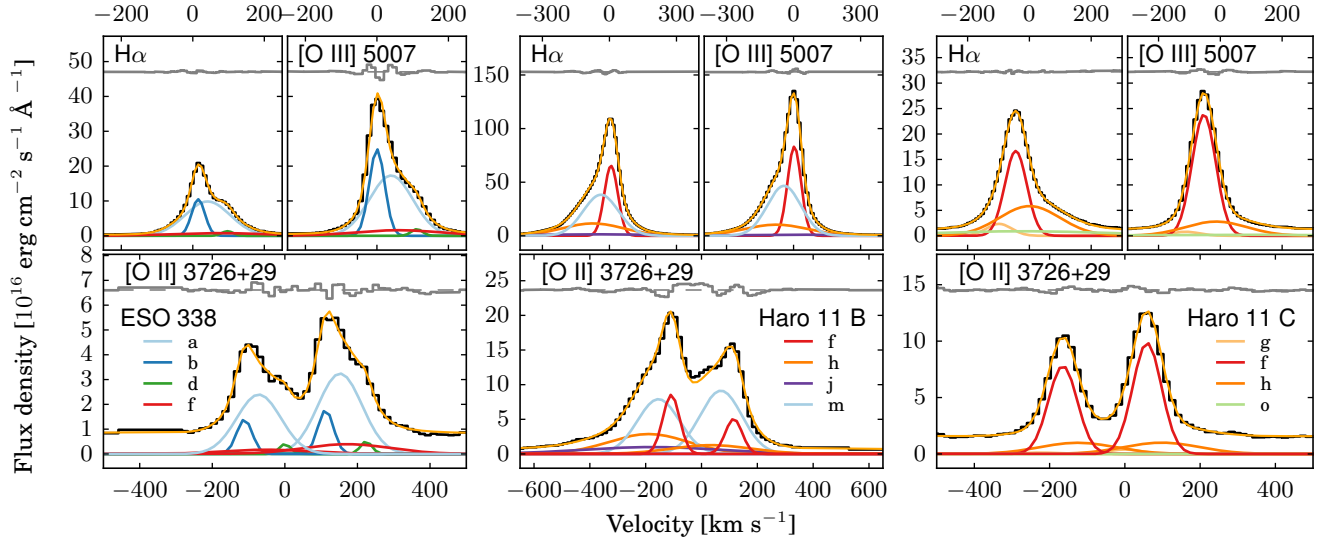


Figure 8. Model of the row containing the strongest $H\alpha$ emission of ESO 338-IG04; row 39. The model is shown in $H\alpha$, in which it is constructed, as well as in $[O III] 5007$, and in the $[O II] 3726+29$ doublet. The observed profile is shown in black, the individual kinematic components are color coded according to the key shown in the lower panel, and the resulting model shown in orange. Above each profile, in gray, residuals are shown to scale around an offset zero-level. Point to figures in later chapter where fit parameters are shown.

components of low flux compared to the line total tends to lead to a large scatter in all of the three fitted parameters A , v and σ . Thus, our ambition in this work has been to identify and track the most important components, knowing that some comparatively minor, but significant, portions of flux may have been left unaccounted for.

As an example, figure 8 shows the model of of the three targets in the row of their respective maximum $H\alpha$ flux, modelled in $H\alpha$, $[O III] 5007$ and $[O II] 3726+29$. It is clear from inspection that the model provides a good approximation to the observed data also in $O III$. However, due to the very high SNR, the residuals (shown in gray above the line profile) in some places exceed 20σ , rendering the interpretation of reduced χ^2 and error-scaled residuals ambiguous and potentially misleading as a measure of goodness-of-fit, which is further exacerbated by the centroid velocities and line widths being fixed at or tightly constrained around the values derived from $H\alpha$.

To indicate the quality of our models, we have therefore opted for showing the residuals in terms of the observed spectrum, encoding how large a fraction of the flux in each pixel is unaccounted for by the model, rather than the usual standard deviation-weighted residuals. Maps of these residuals are shown in appendix B.1

3.3.2. Uncertainty estimates

In line with the reasoning in section 3.3.1, the added constraints of consistency within spatial regions and the tight constraining of line width and centroid velocity in

all lines but $H\alpha$ also renders the confidence intervals on Gaussian parameters as reported by the fitting software hard to interpret and potentially misleading as indicators of confidence intervals. The large number of measurements on the other hand allows us to take a more data-driven approach by using the scatter in a given parameter as a measure of its uncertainty.

Summarized in brief, the error bars we report for the weighted average properties for each physical subsystem were found as follows: for each quantity in each labelled component, we first separate deterministic variation (which we interpret as a physical property intrinsic to the object) from scatter, using a Robust Locally-Weighted Regression (LOESS), and since use the bisquare-truncated scatter in said quantity to denote the confidence intervals. On simulated data, the derived value fell within these error bars from the true value $\approx 85\%$ of the time, meaning that they signify $\sim \pm 1.5\sigma$. The procedure is explained in greater detail in appendix B.2.

4. RESULTS

4.1. Kinematic models

Panels (1), (2) and (3) of figures 10, 11 and 12 show the values arrived upon for $H\alpha$ in ESO 338, Haro 11 B and Haro 11 C, respectively. In all panels, the y axis values show the number pixel row along the slit, while the x axis shows model centroid velocity ((1)), peak flux density ((2)), and line width σ ((3)) for each component. Colors reflect assigned label as described in sect. 3.2, according to legend given in the bottom of the figures.

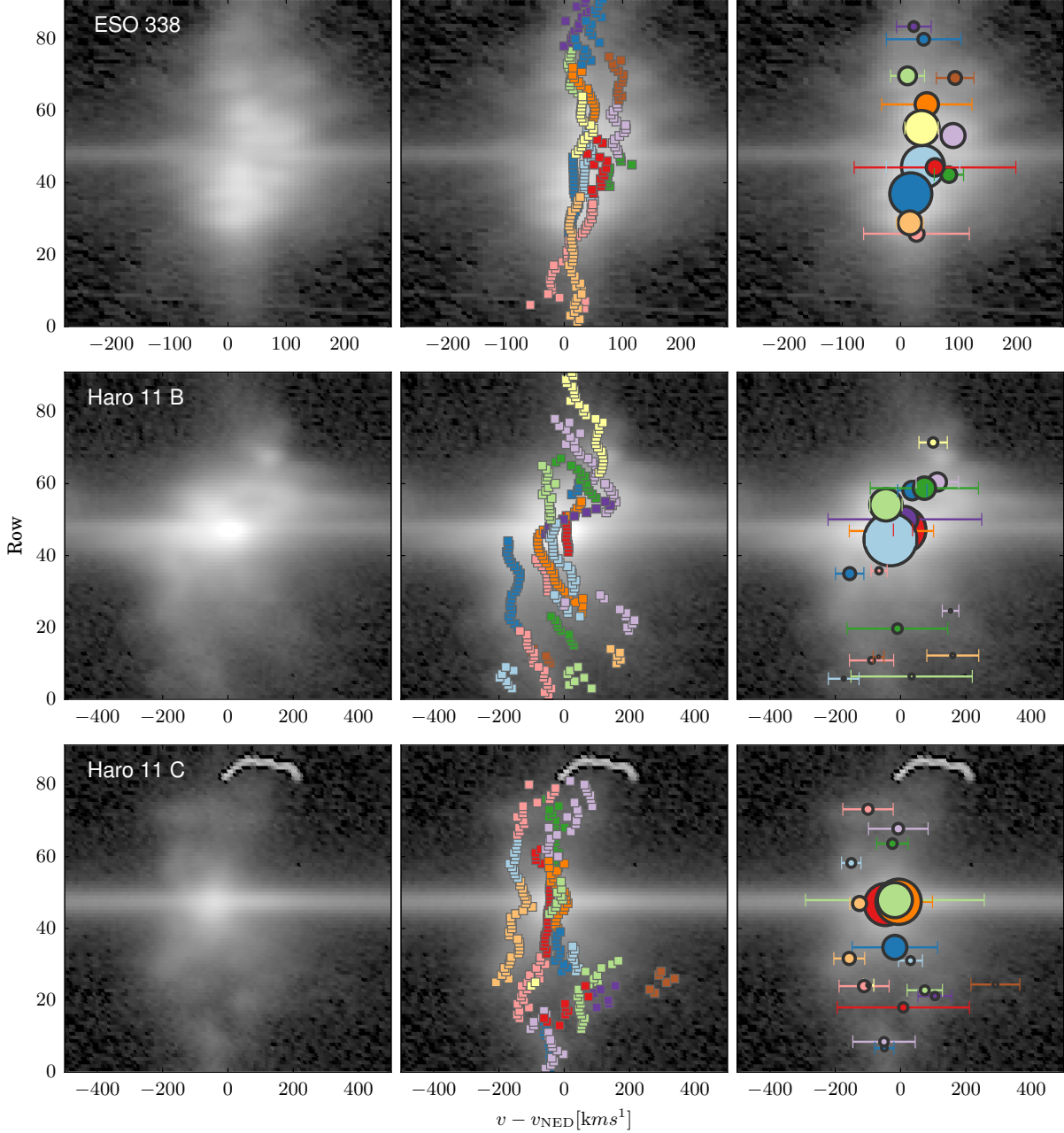


Figure 9. Overview of kinematic components for the three targets **Left panels** show the 2D profile of $H\alpha$. **Middle panels** show the same, with centroids of the model components overlaid, color coded according to their assigned labels. In the **right panel**, circles mark the flux-weighted positions of the component centers. Colors reflect the labels as in the middle panel. The circles are scaled so their areas encode the total flux of each component, and horizontal error bars show the flux-averaged line width in each component. The fluxes are not to scale between the targets.

The central, gray shaded region in each panel shows the approximate extent of the continuum trace of each object. The contents of the remaining frames in the figures are explained in the following sections.

4.2. Derived properties

We have computed a number of line ratio-based parameters and diagnostics commonly reported in the literature, both for each kinematic component and a flux-

weighted average for each physical subsystem. The lines were first corrected for Galactic dust reddening using a standard CCM law (Cardelli et al. 1989) and assuming extinction coefficients from (Schlegel et al. 1998) of 0.0862 and 0.0112 for ESO 338 and Haro 11, respectively, and a standard $R_V = 3.1$.

In figures 10, 11, and 12, some of these properties are shown in panels (4) - (11). Panels (4) show the flux of each component and each row as small squares, color

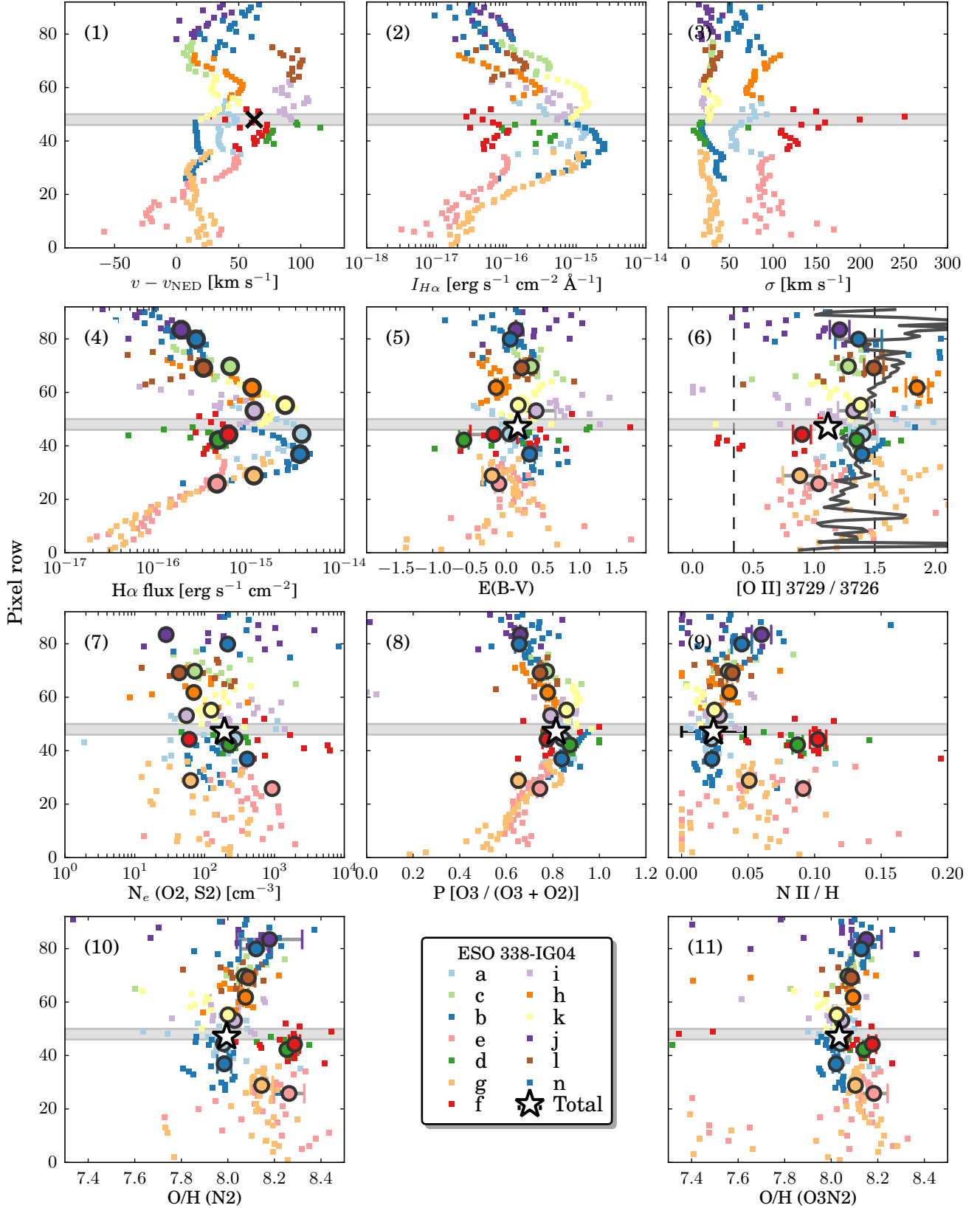


Figure 10. Overview of fitted model parameters and derived quantities for each component in ESO 338. In all panels, a **colored square** represents a value for one component in one row, while a **color-filled black circle** represents the flux-weighted average over each subsystem of the same value. Where present, a **full black line** shows the value of same parameter for the entire integrated line feature in a given row. The central **gray shaded region** in each frames shows the approximate extent of the continuum trace. **Black dashed lines** in the $[\text{O II}]$ line ratio map mark the theoretical line ratios from (Osterbrock & Ferland 2006) in the high- and low-density limits. In all frames, numbers on the y axis denote the pixel row number along the synthesized slit, counting from S to N. The black cross in panel (1) shows the stellar velocity.

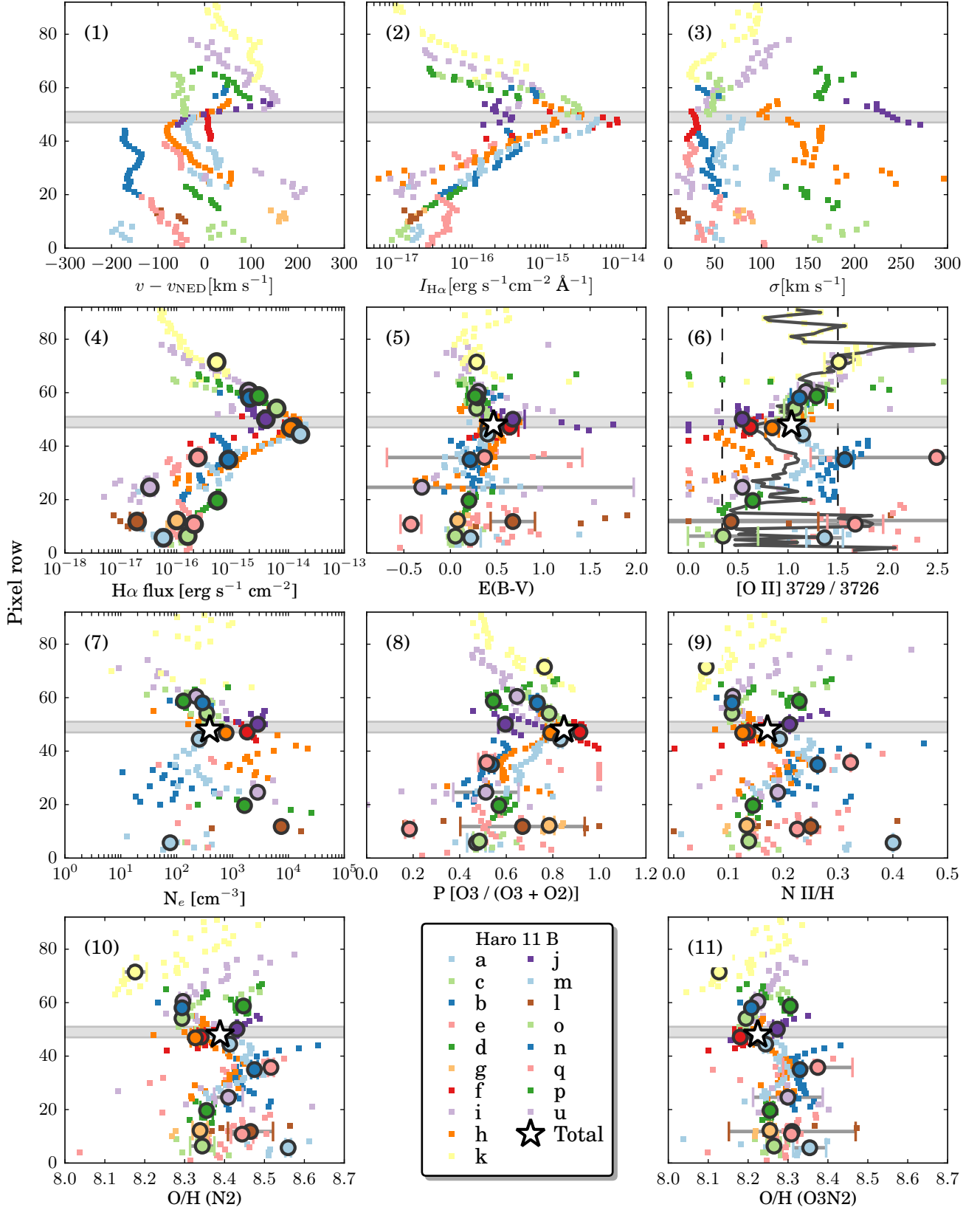


Figure 11. Same as figure 10, but for Haro 11 B. No stellar velocity is given here.

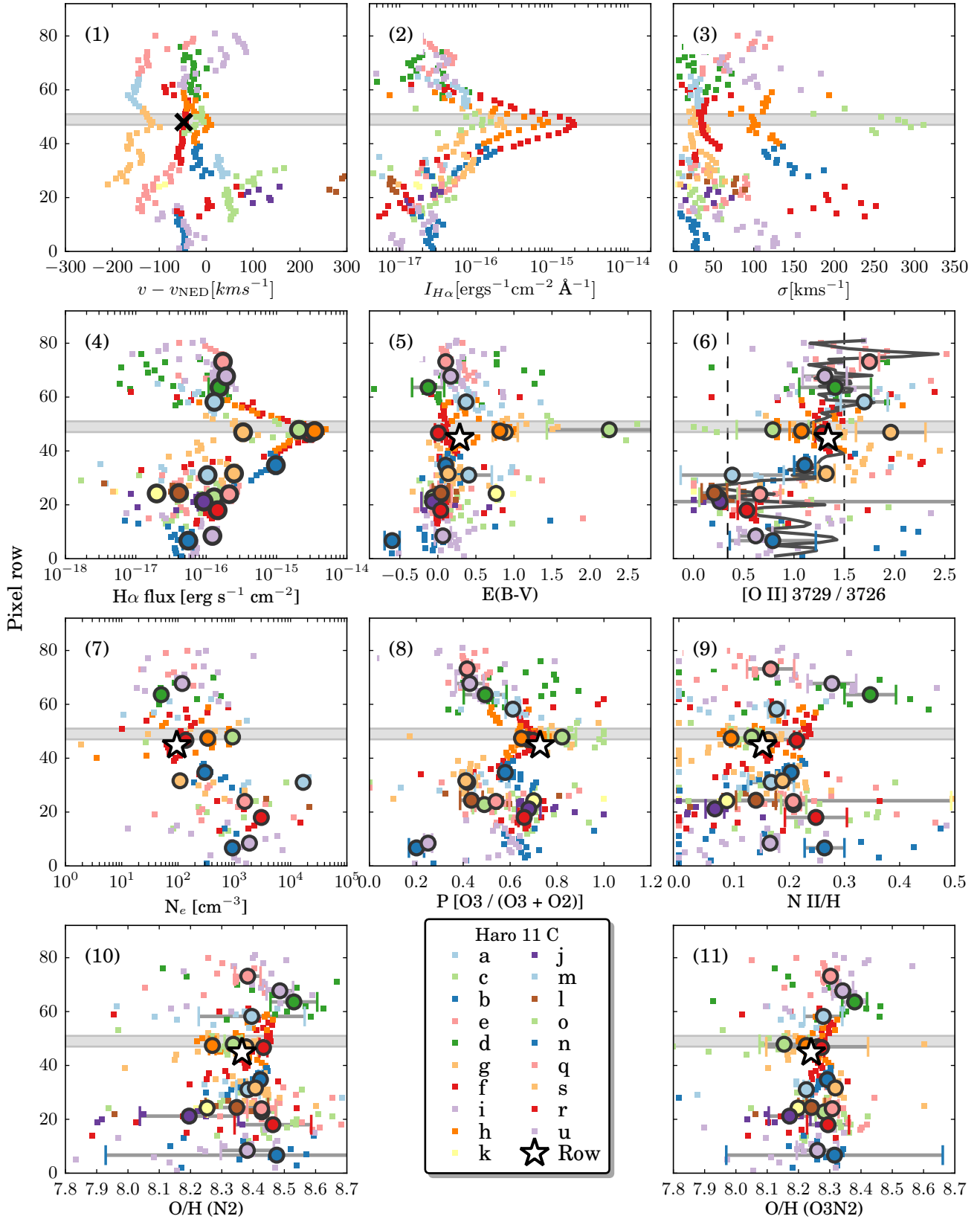


Figure 12. Same as figure 10 and 11, but for Haro 11 C.

coded as explained above. Additionally, the average flux for each component is shown as a larger, colored circle. Error bars are set as described in sect. 3.3.2. Panels (5) show the color excess $E(B - V)$ computed from the Balmer decrement. Values are shown as they are found; negative reddening is unphysical and should be interpreted as zero. Circles denote the average for each component, with contributions from each row weighted by the flux in $H\alpha$ for said row and component. Finally, the global average, taken over all rows and components and weighted by $H\alpha$ flux, is shown as a white star. The decrements are found assuming a Calzetti attenuation law (Calzetti et al. 2000).

Panels (6) show $[O II] \lambda\lambda 3729/3726$ line ratio, with symbols and colors as before. Vertical dashed lines denotes the limits of the region, within which electron density can be computed from this ratio according to (Osterbrock & Ferland 2006). The full black curve shows the value computed by combining all components in each row. Electron densities computed from these ratios, where possible, are shown in frames (7); for Haro 11, these are computed with the PyNeb `getTemDen` method, assuming an electron temperature of $T_e = 10^4 K$, since no temperature sensitive line was strong enough to measure the temperature directly outside the central sources. See sect. 4.3 for a description of the procedure for ESO 338.

In panels (8), we show the ionization parameter given as

$$P = I(5007)/[I(5007) + I(3726 + 3729)],$$

encoding the fraction of ionized oxygen which is in the doubly-ionized state.

Panels (9) contain the ratio $I([N II]6583)/I(H\alpha)$. Panels (10) and (11) contain oxygen abundances $12 + \log(O/H)$ found by empirical strong-line diagnostics typically used in the absence of faint temperature-dependent emission lines like $[O III] \lambda 4363$. The diagnostics chosen here are the $N2$ method and the $O3N2$ method, using the calibrations by Marino et al. (2013). Another common method, the R_{23} method, was decided against as it is double-valued with its peak near $12 + \log(O/H) \approx 8.0$, which according to the other methods is close enough to the values of these galaxies to render the method unreliable.

4.3. ESO 338-IG04: $[S II]$ and auroral $[O III]$

For ESO 338, the $[S II] \lambda\lambda 6717, 6731$ doublet is free of the telluric absorption lines which partially cover it in the case of Haro 11. This provides us an independent measure of the N_e for this spectrum through the flux ratio of these lines. This flux ratio is shown in the same manner as in fig. 10 in panel (1) of figure 13. As for the $[O II]$ line ratios, the black curve traces the values for

the integrated lines in each row, and the vertical, black dashed lines mark the upper and lower theoretical limits of line ratios that can be mapped into electron densities according to Osterbrock & Ferland (2006). These line ratios are significantly less noisy than those of Oxygen, but agree in the overall trend of generally having high line ratios, corresponding to low electron densities, except in component f (red), which is consistently denser. Components e and g (pink and light orange) show low line ratios in Oxygen, but high line ratios, and lower scatter, in Sulphur. The S II lines have significantly better sampling, smoother continuum and better line separation than O II, meaning that the S II line ratios are probably more reliable despite a somewhat lower SNR. Component d (green), on the other hand, behaves the opposite way. This component is central and has decent S/N in both doublets, so it is difficult to say which line ratio is more reliable as a measure of N_e in this case. Also the overall, integrated line ratios differ visibly.

The auroral line of $[O III] \lambda 4363$ is detected in the central cluster of all three targets, but only detected in extended emission for ESO 338, where it allows us to trace the kinematically decomposed electron temperature out to $\sim \pm 4''$, which corresponds to $\approx \pm 800$ pc. at the distance to ESO 338. This also provides an opportunity to directly determine Oxygen abundance and compare it to the empirical strong-line diagnostics on which we otherwise rely.

With both the singly-ionized Sulphur and Oxygen doublets and the auroral Oxygen line measured, we can compute the electron density and temperature in two and three different ways, respectively. Firstly, we used the software package PyNeb (Luridiana et al. 2015), which contains the `getCrossTemDen` method, which iteratively finds the best values of temperature and density from a pair of line ratios sensitive to each of these properties. For a temperature sensitive ratio we used $[O III]_{4363}/([O III]_{4959} + [O III]_{5007})$. We performed two independent calculations, based on the $[S II]$ and $[O II]$ ratios. Furthermore, we computed T_e directly, assuming an electron density of $n_e = 10^4 \text{ cm}^{-3}$, a high value for the warm medium yet still low enough that its effects on electron temperature are weak, giving us three values of T_e and two for N_e .

Densities reported in panel (7) of figure 10 are averages of the ones found with PyNeb. Temperatures are averages where there is reasonable agreement between the three values. In some cases, there were good agreement between two while the third was in very poor agreement with these. In such cases, the outlier was rejected and an average of the remaining values reported. This was the case for components e (pink), for which PyNeb arrived at unrealistically high temperatures of $T \sim 10^5 K$, and for component f (red), for which `abund` arrived at a

similarly unrealistic value. This component also seems to have problems with the density estimate, for which the averaged value is much lower than the values of the single component, and similarly the pressure is lower. Similar density problems may be at play for components *b* and *i* (dark blue and light purple).

Electron density is thus the only quantity in fig. 10 which is computed in a different way for ESO 338 than for Haro 11. Electron temperature is shown in panel (2) of fig. 13, with the usual notation. In the upper and lower ends of the slit, [O III] $\lambda 4363$ is so faint that the computations break down and yield an unrealistically low temperature. However, since these components in these rows also carry very little flux in $H\alpha$, this has only a small impact on the weighted averages, which are dominated by relatively few rows with higher flux in both transitions.

The integrated value for the entire spectrum is reported in table 4.4, where errors are computed by standard propagation of uncertainties. The value arrived upon here is found to be within 2.5% of that found by (Guseva et al. 2012), although arrived at slightly differently. We can however see from panel (2) in fig. 13 that this temperature covers a range of temperatures, from ~ 12000 K in the surrounding gas to ~ 22000 K in the central cluster. The temperature depends almost solely on the distance from the central cluster; there is little variation between kinematic components with the exception of component *f* (red). This component is spatially and kinematically coincident with the stellar population in the main cluster (see panel (1), fig. 10) and is the broadest of all components, together suggesting that it does indeed reside in or near the central cluster; see further discussion in sect. 5.

Panel (3) in fig. 13 shows the gas pressure in units of $K \times \text{cm}^{-3}$ (that is, with $R = 1$). It shows a weak rising trend from N to S, as should be expected from the rising density and almost constant temperature.

In panel (4), the figure shows the O/H metallicity derived from the direct T_e -method. As with the temperature, because of the faint [O III] $\lambda 4363$ line in the outer parts (where it is essentially zero), the individual rows here show an enormous scatter. However, because these components in these rows also carries little flux in $H\alpha$, the weighted averages are not very strongly affected by this. These metallicities also provide a basis of comparison for the metallicities derived from the strong-line diagnostics described below. Panels (5) and (6) show oxygen abundances by O3N2 and N2 methods, respectively, plotted against abundances found by the direct method. The Dashed line shows the 1:1 locus; only averages are shown here.

The last two panels show, on a y -scale given to the right, scatter plots of the averaged, empirical strong-

line abundances vs. the directly determined ones. Diagonal line marks the 1:1 relation. Note that while the values (except for one, which we have already marked as suspicious above) agree fairly well, there is not actual correlation between them. It appears one should be careful about using the empirical strong-line methods to compute internal variations in metallicity in a galaxy; as these methods rely on N/O being constant, while in reality it clearly varies.

4.4. Global values

For each of the quantities described above, we have also computed a global value, averaged over all components with $H\alpha$ fluxes as weights in the usual way. While we have seen that these values cover a wide underlying variety of physical conditions, they do serve as basis for comparison to quantities found in the literature. A selection is presented in table 4.4.

Table 3. Integrated properties

| Quantity | ESO 338-IG04 | Haro 11 B | Haro 11 C |
|-----------------------|---------------------|-------------------|-------------------|
| (1) | (2) | (3) | (4) |
| $E(B - V)$ | 0.155 ± 0.003 | 0.463 ± 0.007 | 0.267 ± 0.009 |
| T_e | 14430 ± 40 | ... | ... |
| N_e | 192 | 389 | 95 |
| p [$\times 10^6$] | 2.772 ± 0.008 | ... | ... |
| P | 0.814 ± 0.006 | 0.848 ± 0.001 | 0.728 ± 0.004 |
| [N II]/ $H\alpha$ | 0.0240 ± 0.0003 | 0.171 ± 0.002 | 0.152 ± 0.002 |
| O/ H_{T_e} | 7.89 ± 0.01 | ... | ... |
| O/ H_{N2} | 7.995 ± 0.003 | 8.389 ± 0.002 | 8.365 ± 0.003 |
| O/ H_{O3N2} | 8.035 ± 0.001 | 8.224 ± 0.001 | 8.243 ± 0.002 |

We note that the value we find for $12 + \log(O/H)[T_e]$ for ESO 338 is identical to the value reported by Guseva et al. (2012), and the strong-line diagnostics we find are generally within 0.10 - 0.15 dex from the T_e based values found therein. We refer to their article for a number of literature values for comparison.

4.5. BPT analysis

With the kinematic decomposition in place, we can also investigate the question of whether single components seem to be subject to shocks, hard radiation etc. It is well established that the galaxies in question are overall consistent with ionization being driven purely by star formation (Guseva et al. 2012; Leitert et al. 2013); however, starburst galaxies contain a wide variety of physical conditions, and some components, while not

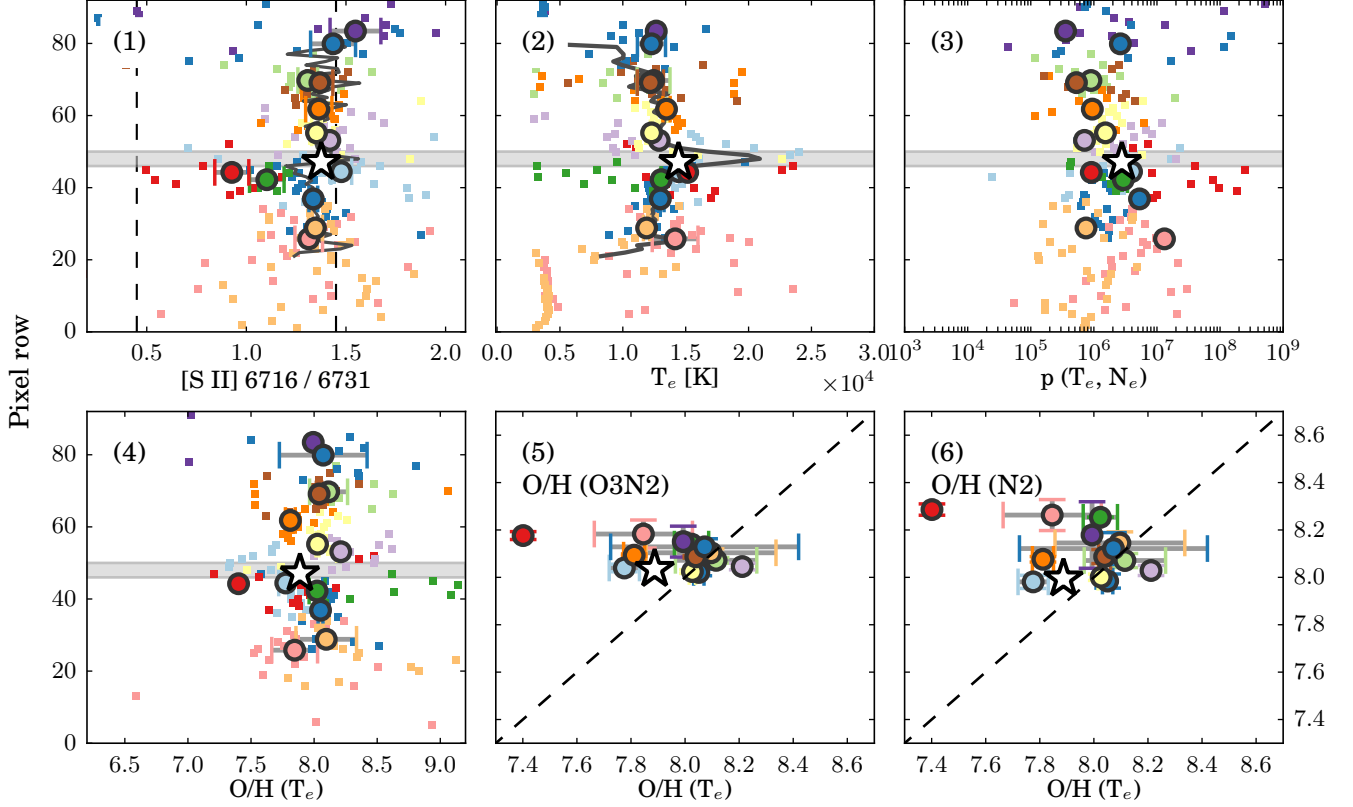


Figure 13. Parameters only measured and derived in the case of ESO 338-IG04. Apart from the [S II] doublet at $\lambda\lambda$ 6717+31, these are all dependent on the temperature sensitive [O III] line at λ 4363 Å. Panels (5) and (6) compare O/H by the direct method to the two empirical diagnostics of panels (10) and (11) in fig. 10. The dashed lines show identity. The y-axis values for these panels are shown to the right on the figure.

dominating the overall flux of the galaxy or starburst region, may still individually have line ratios deviating from this agreement. To this end, we have performed an analysis of the individual components based on the Baldwin, Philips & Terlevich (BPT, Baldwin et al. 1981) classification scheme.

The diagram in fig. 14 gives a good basis for comparison between the three targets, as well as an overview of the scatter in physical conditions that are usually contained in one single number. The scatter is considerable, confirming that these galaxies contain a wide variety of physical conditions. We see that both ESO 338 and Haro 11 C lie comfortably in the HII region part of the diagram on the left side, although a few integrated components lie in the composite region and one single integrated component of Haro 11 C in fact lies above both the Ka03 and Ke01 lines. Perhaps more interestingly, the integrated Haro 11 B lies in the composite region between the two lines, suggesting that although it is not dominating, a component of the light is not photoionized by star formation. Like knot C, this knot also has one single integrated component lying above the Ke01 and Ka03 lines, and a number of others falling in the

composite region.

In the right panel, it is interesting to see that the [O I] 6300 / $H\alpha$ ratio puts several averaged components well into Seyfert territory. The fact that the total, integrated values stay well in the HII region part of the diagram however shows that the components on the right have low flux, and are more likely to be heated by some other kind of hard UV spectrum or shock; while the [O III] 5007 / $H\beta$ ratio is sensitive to the strength of the ionizing field, the [O I] / $H\alpha$ ratio is sensitive to shocks and the hardness of the ionizing field (Kewley et al. 2006), so shocks or a faint but hard component could place smaller amounts of gas in the LINER or lower Seyfert domain.

To investigate more deeply which gas phases are present where, we produced BPT plots by spatial regions of 10 pixel rows, color coded by component. One such plot for Haro 11 B is shown in figure 15. The Ke01 and Ka03 lines are included as before, and error bars are here simply the propagated uncertainties on the component fluxes. The regions overlap by one row. With the less overwhelming amount of information present in each frame, it now becomes apparent that while there is some scatter especially in the fainter components in

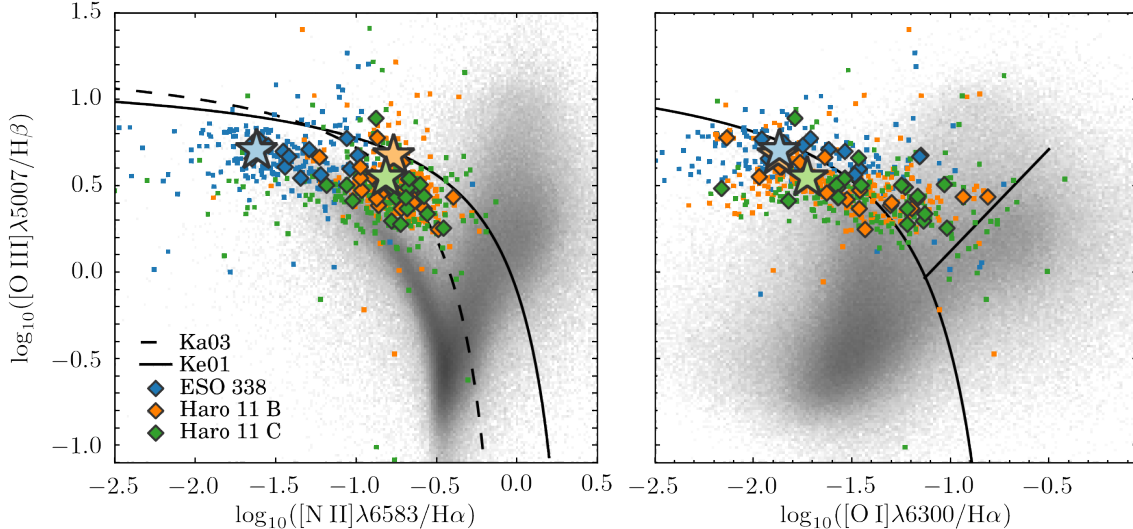


Figure 14. BPT diagrams of the three targets. **Left panel:** The classification scheme of (Kewley et al. 2001), with the theoretical upper limit for strong starbursts as a full black line. The empirical lower limit for AGN components of (Kauffmann et al. 2003) is drawn as a dashed black line. The background, grayscale histogram shows the density of objects in SDSS DR7 in this classification scheme. Single-row components are shown as colored squares, flux-averaged subsystems as filled diamonds, and the total flux-averages over the collapsed slit are shown as stars in corresponding colors. **Right panel:** The [O I] λ 6300-based classification of (Kewley et al. 2006), with the starburst/AGN division curve and the straight Seyfert 2 / LINER division line both shown as full black curves.

the upper and lower ends of the slit, the behavior of the components is generally coherent and well behaved.

One noteworthy feature is component f , which lies consistently above both the classification lines by $\sim 2 - 3\sigma$; only one point falls in the H II region part of the diagram, and that one has enormous horizontal error bars - the only part of it visible in the central panel. The component is accompanied by another, j , which has parts both above and below the division line. However, the parts of it in the range between rows 40 and 49 is consistently in the upper part, while the part in rows 50-60 is consistently in the composite region, suggesting that the physical conditions in the component do indeed change with distance from the central source. Also component m , the one component with the strongest flux in $H\alpha$ and kinematically closest to f and j , resides consistently in the upper part of the composite region over a range of ~ 15 rows.

Knot C too has one component, o , associated with the central cluster, which resides consistently above the separation lines of the diagram, in fact by a more convincing margin than that of comp. f in knot B. However, o in knot C has a strong scatter and large error bars. Furthermore, knot C was the only system with stellar absorption in $H\beta$ strong enough to prompt correction. Component o is faint in peak strength but very wide, the very kind of component most vulnerable to systematic uncertainties stemming from the absorption correction in $H\beta$, uncertainties that carry through in

the division. In contrast, knot B had negligible stellar absorption even in $H\gamma$, its component f is narrow and extremely bright, and the fluxes even in the broad and faint component j well determined.

Also ESO 338 has a narrow component d which sits consistently on or right above the separation lines (which are practically coincident at its modest N II abundance), accompanied by a broader line f which shifts between the composite and upper region. These lines are however both quite faint and less well defined. On the other hand, by the O I - vs. - O III diagnostics, both of these components in ESO 338 also reside solidly inside the Seyfert region of the diagram. In contrast, components f and j in Haro 11 B both sit in the HII region part by this diagnostic, albeit close to the separation line. For knot C, component o again falls above the separation lines, but with very large scatter and error bars. This target has the faintest O I outside the central region of the three.

4.6. Haro 11: Slit overlap

The two slit coverage areas in Haro 11 overlap (see fig. 1), the overlap region is centered on row 24 (29) in knot B (C). In this region, data and hence model should be roughly the same although not identical: Slit positions are only approximately known, and even with the slit position known with perfect precision, the difference in slit and dispersion angle means that even the rows in center of the overlap region sample overlapping but dif-

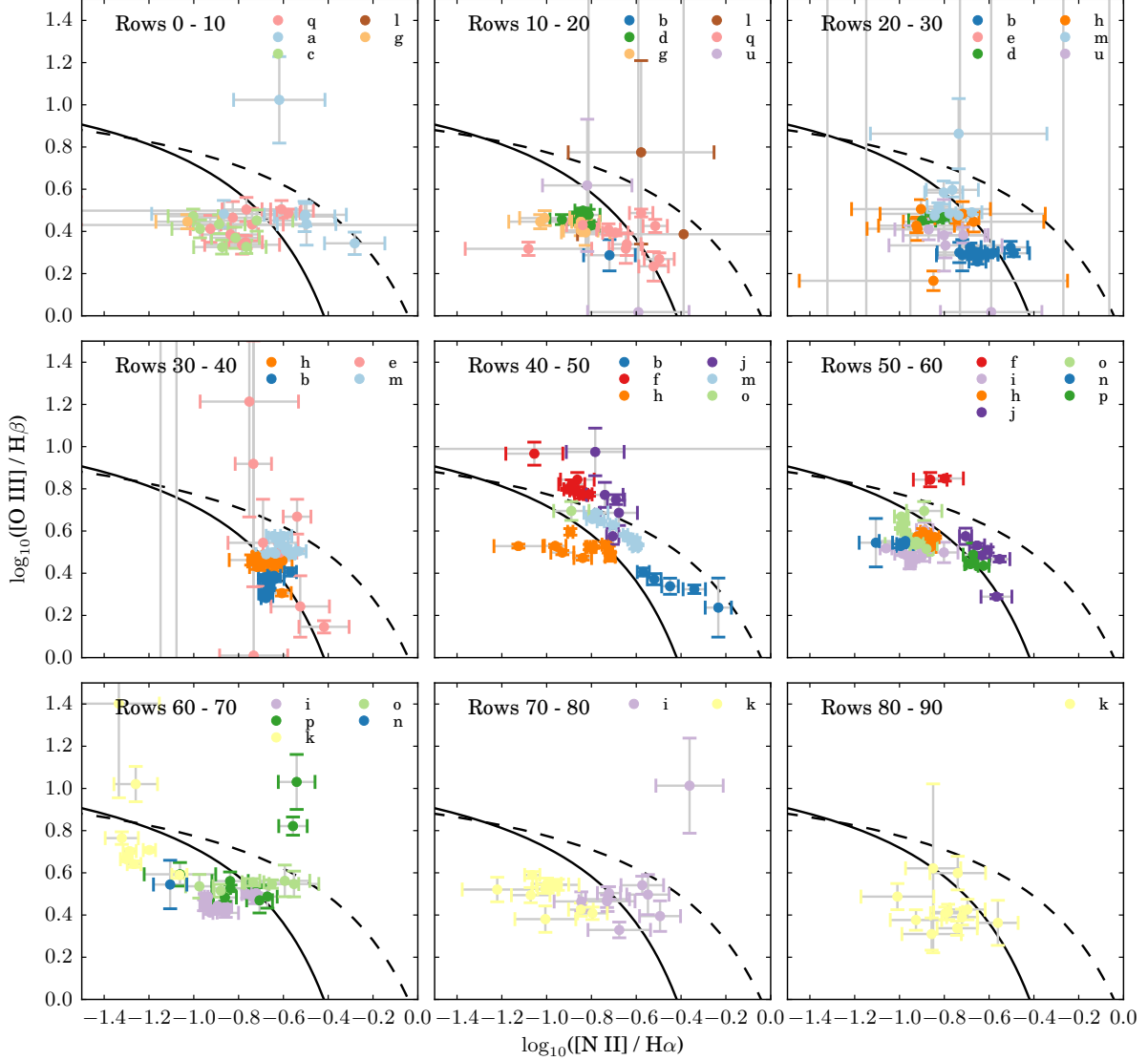


Figure 15. BPT-diagram of individual row-components for the slit at Haro 11 B in sections of 10 detector rows, color coded by component. Error bars are propagated standard deviation estimates from line fitting.

ferent spatial regions. Still, checking data and derived models for consistency in this area is a useful test of the validity and possible limitations of our method.

Data in the two spectra are similar in line shape, but the peak flux in Haro 11 B row 24 is around 40% higher than in Haro 11 C row 29. The mismatch is probably not due to differences in flux calibration; the continuum levels are consistent, so it is more likely a difference in the region sampled. In slit B row 23, the difference in peak intensity from slit C row 29 is only $\sim 10\%$. This shows that conditions can vary rapidly over short distances, and hence we should also expect non-negligible effects of the difference in slit angle.

The model profile in both cases consists of a few strong peaks at roughly similar velocity and width, and a few smaller bumps. However, there are differences too, the

most conspicuous being a faint, broad component found in slit B but not in slit C, possibly due to the poorer SNR in the data for slit C.

The models fit consistently well in adjacent rows within each spectrum, while we could not make the minimizer settle on a slit C-like model with the data of slit B, or vice versa. With a seeing being low but varying between the two observations, and the accuracy of the slit placement being unknown, it is likely that the difference in model actually reflects a combination of different SNR, slit orientation and placement, and the models being simplified representations of the underlying physical systems which, we should note, seem particularly complex in this region.

5. DISCUSSION & PHYSICAL INTERPRETATION

We shall now attempt to combine the findings of the previous sections, as well as others from the extensive literature on these galaxies, into a coherent picture of the conditions in and properties of their warm interstellar gas.

5.1. *ESO 338*

ESO 338 is dominated by the large central supercluster, Cluster 23. Figure 1, left panel, shows clearly how feedback from the cluster has blown a bubble in the surrounding gas. Östlin et al. (2007) describe how the surrounding bubble, which they estimate to be around $1''$ or ~ 100 pc in diameter, is expanding at a velocity of $v \sim 40$ km s $^{-1}$. At the same time, in fig. 1 can be seen how the warm H α emitting gas forms an extended filamentary and clumpy structure in the entire length of the slit (and beyond).

Considering the kinematic model, shown in fig. 10 panels (1)-(3), we first note that the intensity of H α is strongest above and especially below the central cluster, in which it dips to a level close to that of the stellar continuum. The luminosity of H α in the central cluster is in fact so low that the ratio of $L\alpha/H\alpha$ in this region gets above Case B recombination levels (Östlin et al. 2009), possibly because Ly α from other regions scatters into the LOS while very little Ly α or H α originates there. The region around the central cluster also contains the only gas which has close to zero velocity relative to its stars, *d* and *f*. These are very narrow and very broad, respectively, but both have relatively low flux in H β . For the rest, the components fall into three groups. One group is broad, with line widths between 60 and 100 km s $^{-1}$. These components are outflowing from the cluster by ~ 20 km s $^{-1}$, growing to larger velocities in the northern and especially the southern end of the slit. In addition, we see two groups of narrow components, 30-50 km s $^{-1}$, which are flowing away from the cluster at roughly 50 km s $^{-1}$ in both directions along the LOS. The narrow lines have a width consistent with being single HII regions, while the broader lines are likely to be made up of a number of fainter systems. The narrow lines are also the most luminous, and likely correspond to the H α emitting regions shown in red in fig. 1. From this, and their seemingly symmetric velocities around Cluster 23, we interpret these regions as the boundaries between a large central cavity around the cluster and the surrounding, denser and cooler gas. The broader components have line widths which are unlikely to be due to thermal broadening and thus are probably each made up of several low-luminosity subsystems, moving in the gravitational potential around the cluster, which could both explain their line widths and that their velocity centroids are sandwiched between those of the luminous narrow boundary regions. The positive velocity of these

components relative to the cluster could be due to either large scale motion due to an earlier interaction, or an asymmetric gas distribution being radially pushed by feedback from the central cluster. We interpret at least the strong velocity gradient in comp. *e* (pink) as due to a large scale outflow extending to the S.

The narrow components on the receding side are detected as far as 20-25 pixel rows, corresponding to $3.2 - 4''$ or roughly 600-800 pc, to the north of the central cluster. Beyond this point the H α flux in general drops off, and the velocities of the components approach that of the cluster. The approaching set of narrow lines have the majority of their flux in the central half of the slit, but are detected in its entire length. The extent of the receding components, taken together with the HST imaging, suggest that this cavity extends out to ~ 600 pc., around the 28 s mark in the left panel of fig.1. Both the broader and the narrower components become very luminous in H α on the south side of the cluster, probably reflecting a denser gas, which could possibly be opaque to or drown out the contribution from a receding component at this position, if one exists. The majority of the flux from these components falls within 400-600 pc., which also from the imaging seems to be the southern edge of the larger bubble, which in the HST image seems to be limited by the easternmost vertical string of hot clusters, and to the West approximately at the 58.00 s RA mark. Looking at fig. 10, panel 8, shows that the ionization parameter *P* generally varies smoothly with distance from the central cluster.

5.1.1. *Dust reddening*

One original motivation for this study was to attempt using dust reddening as a proxy of physical depth to take clues about the three dimensional structure of the targets. For ESO 338, we first note that the found values of $E(B - V)$ are very low, often unphysically so, and mostly consistent with zero. Furthermore, it is not immediately clear how to interpret the found values. The two receding components furthest to the N, *a* (light blue) and *l* (brown), both have $E(B - V) > 0$, but the latter is less reddened than component *c* (light green), supposedly lying in front of it; and component *b* (blue), by kinematics suggested to lie in front of the others, is the most strongly reddened component S of the cluster.

The lesson to learn from dust reddening could be that the actual gas and velocity distribution is more complex and possibly randomized than our interpretation implies. However, using $E(B - V)$ as a proxy of depth rests of the assumption that dust is more or less homogeneously distributed, an assumption which may break down at the angular scale of a slit width. Dust lanes visible in Haro 11 in fig. 1 suggests that small-scale structures are present. If these have a geometry which covers

some components in a given detector row more than others, this could have a randomizing effect on the depth inferred from reddening.

5.1.2. Density, temperature & pressure

Density estimates for this system are messy, as there is a large scatter in the [O II] line ratios. Specifically, the iterated density of the flux-averaged component f is up to an order of magnitude lower than all its single constituent components, which means it should be taken with caution. If however we adopt the [S II] line ratios as a measure of density, we see a very low density everywhere except in the components f and d which, in combination with [N II]/H α values unusually high for the system, further strengthens the case for their being associated with the central cluster, although the problem of at least d being spatially removed from it by ~ 100 pc still stands. The nitrogen lines are also strong in the southern components e and g , suggesting that they might not fall in line as smoothly as the other components and thus that their higher densities found through the [O II] ratios may hold true.

In panel (3) of fig. 13 it is seen that the pressure in this system is somewhat scattered and also shows a weak gradient from N to S. A rough estimate shows that with a sound speed of ~ 15 km s $^{-1}$, a resolution element of ~ 100 pc has a sound crossing time of ~ 6 -7 Myr. Clusters in the central part of ESO 338 have ages ranging from a few to ~ 30 Myr (Östlin et al. 1998), and feedback sets in after a few Myr, so it should not be surprising to not find pressure equilibrium in this region.

5.1.3. [N II] rich spike feature

One particularly noteworthy feature in this spectrum is the spike structure protruding from the underside of the continuum trace, South and towards the red side, in the N II doublet around H α , most clearly seen in [N II] 6583. Looking at e.g. H α and the [S II] doublet shows that a small feature is visible which could form the base of the spike-feature, but the spike itself is not visible in these lines, or any of the others apart from [N II]. Thus, while the base feature is included in the model as component d , the outer parts are not represented in the model.

A zoom of the feature is shown in figure 16. A rough estimate shows that it spans ~ 220 pc. in the slit direction, and ~ 100 km s $^{-1}$ in velocity space. Assuming that the transverse velocity is the same as the LOS velocity, this gives a travel time of $\sim 2 \pm 0.2$ Myr, or half, if the source is located in the middle, in which case the stronger flux in the upper part could be due to meeting denser gas.

The hinge point of the feature is located at a projected distance of around 100 pc. South of Cluster 23, at

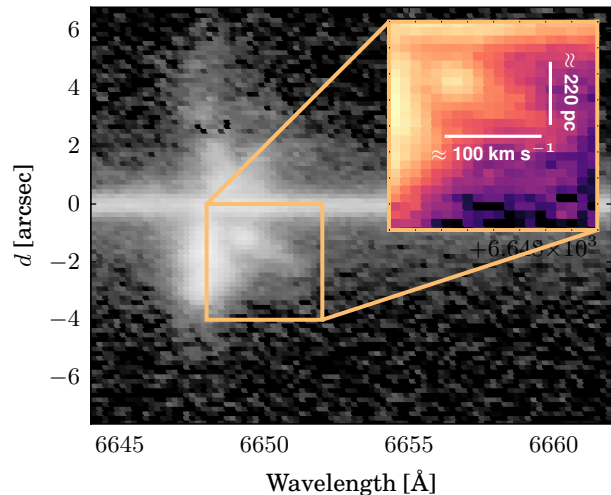


Figure 16. Zoom of the “spike” feature in [N II] of ESO 338, with rough estimates of its extent in velocity and physical space.

the interface between the central bubble and the strong, southern H α gas seen in fig. 1. However, its velocity is consistent with that of the central, stellar cluster and the gas components f and d , rather than the majority of the H α flux which at this location is approaching at $\sim 20 - 50$ km s $^{-1}$ relative to the cluster. Both these components are, as seen in last section, highly ionized and ionized and have [O I] / H α ratios which suggest a strong shock component or hard UV spectrum (both of which this diagnostic is sensitive to), but is incompatible with purely stellar photoionization. It could be a supernova remnant or the combined remnant of several supernovae, although this would be difficult to reconcile with the associated gas component d which at $\sigma \sim 30$ km s $^{-1}$ is closer to that of a typical H II region. We should note that it is possible that they are not actually coincident but merely aligned along the LOS. Another possible explanation is an accreting Black Hole. This could potentially explain why component d is extremely narrow while showing the strongest [O I]/H α ratio, as the latter could then be attributed to the hard UV spectrum rather than an amount of shocks which would otherwise be expected to produce a broad rather than a narrow line feature. See further discussion of the BH hypothesis below.

5.2. Haro 11 B

From the HST imaging in fig. 1, right panel, Haro 11 B is seen to be shrouded in a thick layer of strongly H α emitting gas. Centered around the knot itself is an hourglass-shaped region of star formation activity, visible as a yellow tint, oriented roughly parallel to the slit. A dust lane cuts across just NW of the central

knot, perpendicular to the slit direction. As can be seen in fig. 11, this dust lane is coincident with and probably causing some discontinuities in the model.

Unlike the other targets Haro 11 B shows some clear signs of rotational components, although other components do not follow this motion. The lower, SE end of the slit shows a scatter of minor components with a velocity spread as large as $\sim 400 \text{ km s}^{-1}$, similar to what is seen in the southern end of the slit for knot C, with which this one overlaps. One component, b , is outflowing at slightly less than 200 km s^{-1} ; this component is also present in the central half of the slit for knot C, meaning that it is probably one large structure. The pink component q in the South end connected to component b shifts towards lower velocities towards the end of the slit suggesting that this might be a tidal arm or similar being flung outwards by the merging event. The amount of rotation we find seems consistent with the Fabry-Perot mapping of Östlin et al. (2015), although the complexity in kinematics makes a direct comparison difficult with the single-component fits in this paper.

Components d , h , e , j , i , p , and k (green, orange, pink, purple, light purple, green, and yellow) all show an overall differential rotation-like pattern, although velocities toward the ends seem to even show some counter-rotation. The rotation trend is also broken by components m , f , o , and n (light blue, red, light green and blue). The characteristic ring structure is in the model made up of (parts of) components h , i and n , with component k making up the peak to its immediate North, and component p being the very broad component kinematically and spatially centered inside the ring.

5.2.1. Central components

One component which visually stands out is f , red, in the center. In an otherwise strongly variable velocity landscape, it is practically unchanged across its modest spatially extent. It is very bright in peak luminosity, about twice as bright as its nearest competitor, and very narrow in spatial extent. So narrow, in fact, that it puts an upper limit to the seeing at $\text{H}\alpha$ of ~ 0.7 , compared to a reported DIMM seeing for the observations of around 1.0 (see sect. 2). Its ionization parameter P is the highest in the entire sample, and it has a O III/O II ratio close to 11. With its limited spatial extent, it is consistent with being a point source. It is accompanied by another component of very narrow spatial extent, j , which is extremely broad ($\sigma \sim 250 \text{ km s}^{-1}$) but very faint; and unlike the almost static f component, j shows a continuous velocity shift of $\sim 200 \text{ km s}^{-1}$ over a distance of little more than the width of a seeing disk. Component j has a lower ionization factor than f , but both are, if the [O II] line ratios are reliable, a considerably higher density than their immediate surroundings. The two are

also more strongly reddened than the others, probably at least in part due to a larger fraction of them being obscured by the central dust lane, but also supporting the interpretation that they are associated with the central star cluster.

In the BPT-diagram in fig. 14, we find that component f lies consistently above both the lines of Kewley et al. (2001) and Kauffmann et al. (2003), with a significance of $\sim 2 - 3\sigma$. Also the part of component j which lies below the dust lane around row 50 is consistently above the Kauffmann and Kewley curves, while the part higher up has lower ionization which places it in the composite region. The two components are inconsistent with being ionized by pure stellar photoionization. Shocks by a large number of supernovae would be unlikely to create a line as narrow as f , with a typical $\sigma \sim 25 \text{ km s}^{-1}$. It is also found in our [O I] $\lambda 6300$ based BPT analysis that the lines do not have particularly high fluxes in O I, which would be a tell-tale signature of shocks; and the same components that were unambiguously above the classification curves in the N II based scheme here lie right on top of the separation line, so it is more likely that the ionization source is hard radiation. One option is a population of X-ray binaries, although the point-like extent would require a very concentrated distribution of these, or possibly only one strong source. Another option, which we favor, is that a faint, AGN-like source is present in the central knot.

5.2.2. Hints from X-rays in literature

Haro 11 has been observed in X-rays with Chandra by Grimes et al. (2007), and these data re-analyzed by Prestwich et al. (2015), who find strong X-ray point sources in both knot B and C. Their analysis shows that the point source in knot B, Haro 11 X-1, is extremely luminous, spatially probably a point source, and has a hard X-ray spectrum which they find compatible with either a large stellar-mass X-ray binary, with mass $M \sim 100M_{\odot}$ accreting strongly and seen in what they call the hard mode, implying that we are viewing the accretion disk face-on and directly into the naked source; or with an intermediate-mass black hole (IMBH) with low accretion rate, or a low-luminosity AGN (LLAGN). The latter option they deem implausible based on the lack of evidence for one in optical or IR emission lines. Given that our kinematic decomposition does in fact suggest that an LLAGN could be present, we do not deem this option implausible. An IMBH also seems to be fully consistent with our observations. A single stellar mass black hole does however seem implausible as a source for ionization of component f and j , and in addition, the intermediate- to supermassive black hole scenarios also provide a plausible source driving the expansion that shows as the ring-like feature in our spectra

Haro 11 B

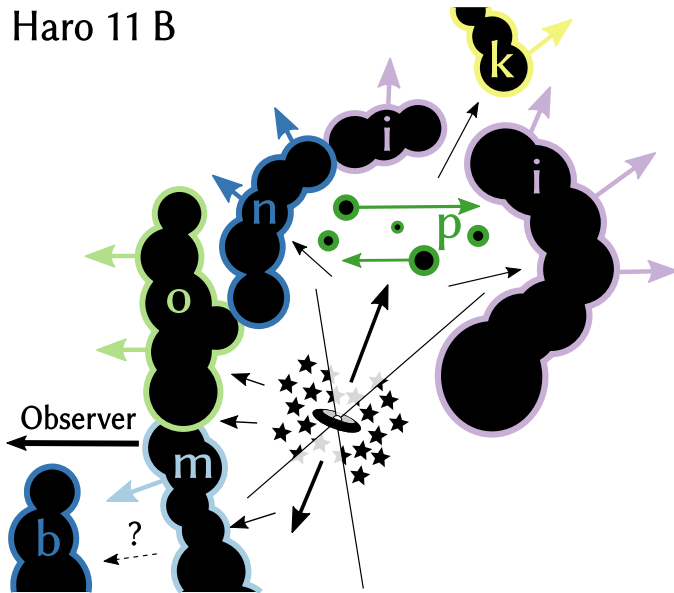


Figure 17. Conceptual sketch of the accreting black hole scenario. Gas clouds are shown in black with lining colored according to the component they are believed to give rise to in the spectra. Colored arrows show the approximate velocity field, while black arrows show how feedback from starburst and black hole impact gas kinematics. Components f and j , both assumed to stem from the central dense region, are omitted for clarity.

immediately to the N of the central cluster. Also Basu-Zych et al. (2016) have analyzed these data, and propose that both these sources are indeed low-luminosity AGN.

5.2.3. Accreting Black Hole scenario

Figure 17 shows a conceptual sketch of how an accreting intermediate or high mass black hole could produce some of the features we see in our model. Black arrows mark momentum and energy deposited by the central starburst and black hole. Gas clouds are shown in black, with edges colored according to the component they are believed to give rise to. Components f and j , both assumed to be associated with the very central region, are omitted for clarity. If an accreting black hole in the central cluster emits its ejecta in a broad cone, as is often found in Type 2 AGN, and the cone is oriented as shown with its axis close to perpendicular to the LOS but with a slight tilt away from the observer in the Northern part, it could induce a close to spherical expansion in a dense gas cloud like the one we observe, with the nearest front at close to the velocity of the cluster. A component like k above the ring could still be both heated and driven kinematically by this, if the cloud is perforated in that direction. The very broad component p , which kinematically and spatially is centered inside this bubble, would in this scenario consist of a number of small gas components driven to high random velocities by the direct influence of the emission cone. Furthermore, frames (1) through (3) in fig. 11 show that components p and j

could well be parts of the same subsystem, given that the transition between them is coincident with the dust lane, which could also be responsible for some of the discontinuity between them. If this is the case, the wide velocity shift in component j would be an expression of matter driven to large velocities by ejecta from the central source; convolution with the seeing could well make this difficult to distinguish from rapid rotation. This hypothesis is strengthened by the observation that these two components, along with component m (light blue) are rich in N II compared to their surroundings. Component m is centered immediately South of the central knot and is slightly blueshifted compared to f , consistent with the orientation of the BH jet, and its velocity drops as its distance from the central source grows. However, the kinematics in this region is complex and nontrivial, so it should be kept in mind that this is indeed speculation.

Haro 11 shows many signs of being a merger system (Östlin et al. 2015). It has been shown by several authors (e.g. Combes 2005; Overzier et al. 2008, 2009) that merger events trigger starbursts by transferring gas to the central regions. Jia et al. (2011) found that LBAs in the ‘Composite’ region of BPT diagrams often showed strong X-ray luminosities, which they interpret as a sign of growing Black Holes. Ellison et al. (2011) found from studies of interacting pairs of galaxies that closely interacting systems more often contain AGN and conclude that it is likely that AGN activity is triggered by the gas being fed to the Black Holes. Basu-Zych et al. (2016) postulate, based in part on these considerations, that the X-ray sources are likely to be ‘hidden AGN’, or weakly or non-accreting SMBHs.

Since the luminosity of an accreting, massive Black Hole depends more on accretion rate than mass, we find no basis in our data to distinguish between these claims. Regardless of the mass, we conjecture that if the current, modest observed activity is indeed triggered by gas fed to the seedling BH by the merger event, then it is possible that this source is currently at the very onset of its activity and could in time turn into a bona fide AGN or a rapidly growing SMBH, depending on its current mass and future accretion rate.

5.3. Haro 11 C

The $H\alpha$ luminosity of knot C is significantly lower than that of knot B. Kinematically, it consists of an outflowing clumpy shell-like structure at around 150 km s^{-1} , or $\sim 100 \text{ km s}^{-1}$ relative to the star cluster and the strongest gas component. This is likely to be the same system which is found SE of knot B, as it is found at the same velocity in the region of slit overlap, meaning that this system is limited, roughly, by the slit overlap, by knot B, and around $4'' \approx 1.7 \text{ kpc}$ N of knot C. Behind

this, the central region is dominated by three components, f , h and o (red, orange and light green) with very different properties but comparable fluxes. Component f is narrow but bright, while o is very broad and faint, and h in between. From fig. 12 we see that components h and o show high dust reddening compared to the rest; however, knot C was the only one with stellar absorption in $H\beta$ strong enough to require correction, and especially component o is broad and faint and thus vulnerable to systematics stemming from the fitting of $H\beta$, so some caution is due when interpreting these. On the other hand, we know from former studies (Hayes et al. 2007; Östlin et al. 2009) that a dust lane crosses the knot in the EW direction, which may affect some components more than others, depending on the geometry on scales below our spatial resolution.

Knot C emits strongly in $Ly\alpha$ (Kunth et al. 2003; Hayes et al. 2007). As several studies have shown, outflows are important to facilitate $Ly\alpha$ escape (Kunth et al. 1998; Atek et al. 2008; Wofford et al. 2013; Rivera-Thorsen et al. 2015), so it is interesting to note that apart from the above mentioned outflowing gas, the majority of line flux in the central region around knot C stems from static or possibly slightly infalling components. Sandberg et al. (2013) found infalling neutral gas by analysis of absorption lines, something which would efficiently block the escape of $Ly\alpha$. We do however see that the ionization parameter in the central region is quite high for all components. In the absence of major cold neutral clouds, this could mean that the majority of gas in this region is ionized and thus transparent to $Ly\alpha$. A secondary component of $Ly\alpha$ emission is found in an hourglass-shaped region around the cluster, axis oriented along the slit direction. Its intensity drops off around $\sim 1.5 - 2''$, or 6-800 pc., above and below the knot, coincident with the ionization parameter P dropping to around 0.4. We suggest that this radiation escapes in a way similar to the off-disk scenario described by Duval et al. (2016), while the higher fraction of neutral gas further out could block any further $Ly\alpha$ escape. Knot C is also believed to be the main source of Lyman Continuum radiation detected to leak from this galaxy (Bergvall et al. 2006; Leitert et al. 2011); this could conceivably leak through a highly ionized medium with few clumps of neutral gas (Verhamme et al. 2015).

5.3.1. Central component

BPT analysis as shown in fig. 15 was performed for this target, too. The flux of both $[N\ II] \lambda 6583$ and $[O\ I] \lambda 6300$ is relatively faint and has low SNR in the outer regions compared to the other targets, so scatter and error bars are large. However, some trends are still visible. Firstly, the N II diagnostics shows only one component, o , which is consistently above the separa-

tion lines. It is generally quite far above them, although it has large error bars compared to the relevant components in e.g. knot B. This trend is even stronger in the O I diagnostic, where this component has an even larger scatter and larger error bars, but also sits even further above the separation line, in the nominal Seyfert region. Unlike the other targets, however, this component is not accompanied by a narrow and equally high-ionized component, and being very broad and strong in the shock-sensitive O I line, this component could well be heated by the shock of strong supernova activity in the central cluster. Like knot B, Prestwich et al. (2015) found that this cluster contains an X-ray point source with a softer spectrum than that of knot B, which they interpret as a slightly above stellar-mass ($20 - 100M_{\odot}$) black hole accreting at super-Eddington rates. Basu-Zych et al. (2016) however suggest that both the sources in Haro 11 are supermassive black holes in a low-accretion state. While our data are consistent with some high-energy processes happening in the cluster center, they do not directly suggest it and give us no basis for preferring one scenario over the other.

5.3.2. Northern shock front

Looking at fig. 5, the flux in all lines drops off rapidly around row number 70-80, after first spreading out in velocity and width. From our BPT-diagrams, we find that while error bars and scatter are large, there is a clear tendency that the lines show low ionization but high O I/ $H\alpha$ ratio, which is indeed suggestive of shocks. If we assume that the almost-static velocities and the fan-shaped $Ly\alpha$ emission is indeed due to an outflow cone with axis close to perpendicular to the LOS, as suggested by Duval et al. (2016), this could be the shock front where this outflow cone hits a denser, not yet ionized surrounding medium. In the Southern end of the slit, the kinematics is, apart from the outflowing system somewhat more complex; velocities stay roughly zero for approximately $3''$, then spread out into two groups of numerous smaller components at $\pm 100\text{ km s}^{-1}$ relative to the central cluster, then converge at roughly zero again at the bottom. Again some sort of expanding shell comes to mind, and it is conceivable that an outflow cone in this direction, if mixing with a more clumpy and less dense medium than in the Northern end, could result in behavior like this, but it is hard to say anything with confidence.

The cluster and the majority of the gas in the Northern and central region, and the average gas in the Southern region, is generally approaching us at a velocity of $\sim 50\text{ km s}^{-1}$ relative to the systemic redshift given in NED. By visual inspection, this is in good agreement with the velocity mapping of Östlin et al. (2015).

6. SUMMARY & CONCLUSIONS

In this work, we have constructed a spatially and kinematically resolved model of the nebular line emission of starburst regions in the nearby Lyman Break Analogs ESO 338-IG04 and Haro 11, which show extended nebulae across almost the entire length of the 14.4'' synthesized slit. We have constructed per-component maps of $E(B - V)$ from Balmer decrement, electron density N_e , ionization parameter P , and empirical Oxygen abundance diagnostics based on the $N2$ and $O3N2$ methods, and for ESO 338, we have constructed maps of electron density T_e from maps of auroral and nebular Oxygen, as well as the Oxygen abundance O/H derived directly from it. Furthermore, for this galaxy we were able to do an independent diagnostic of N_e from flux ratios of the S II doublet at $\lambda\lambda$ 6717, 6731, which fall in a region of telluric absorption for Haro 11. Where possible, we have computed values of these quantities for individual components, as well as global values integrated over all components and detector rows, for comparison with literature values. We have computed a spatial stellar age profile in the central region of the slit for all three targets. We have performed detailed, spatially and kinematically resolved BPT analysis of the targets, which has helped unveil local physical properties which have so far been hidden in previous studies of these targets.

Based on these analyses, careful visual inspection of the 2D spectra and archival HST imaging data, we find the following:

1. All three systems have rich, complex kinematics, inconsistent with a simple large scale ordered motion. Only Haro 11 B shows components consistent with rotation, but this pattern is broken by other, luminous components.
2. We find central ages of the starbursts of $\sim 3 - 4$ Myr. Stellar ages of the surrounding regions were found to be 5.5, 49 and 66 Myr to the North in ESO 338, Haro 11 B and C, respectively; and 6.4, 48, and 42 Myr to the South.
3. ESO 338 shows little variation in electron temperature except in the central cluster and its surrounding bubble. The temperature is $\sim 12,000K$, rising to $\sim 21,000K$ in the central cluster. The doubly-ionized fraction P is in general no less than 0.6, varies quite smoothly with projected distance from the central cluster to a maximum of ~ 0.85 at its highest. The region has a very low metallicity of $12 + \log(O/H) \approx 8.0$ with the exception of one component associated with the central cluster, for which we measure as little as $12 + \log(O/H) \approx 7.4$. This component however is one of four very rich in N II, resulting in $12 + \log(O/H)$ being measured to as much as ≈ 8.3 .

4. Two of the Nitrogen rich components of ESO 338 are kinematically associated with the central cluster, but spatially close to and probably associated to a Nitrogen-rich feature, expanding at a projected velocity of $\sim 50 - 100 \text{ km s}^{-1}$, yielding an approximate age of 1-2 Myr under the assumption of a 45 deg velocity vector angle with the LOS. 1. Kinematics, line strengths and morphology from archival HST imaging suggests that the central cluster in ESO 338 sits inside a highly ionized bubble with a radius of $\sim 100 \text{ pc}$, as found by Östlin et al. (2007), which again sits in an expanding cavity with a radius of $\sim 600 \text{ pc}$, possibly with a projected lily pad like rather than circular shape, with the notch made up of the strong $H\alpha$ feature in the slit immediately below the central cluster.
5. In Haro 11, both slits show evidence of a narrow component outflowing at $\sim 150 - 200 \text{ km s}^{-1}$, independent of the cluster velocities. The component is present even in the slit overlap region and thus likely to be one large component, stretching over at least $\sim 200 \text{ pc}$.
6. Haro 11 B, does, unlike the other targets, show signs of gas rotation, although some components does not comply with this bulk motion. The southern end of the slit is dominated by a number of minor components with a large ($\sim 400 \text{ km s}^{-1}$) and unordered variation in velocity.
7. Component-wise BPT analysis reveals that a strong, static, narrow, point source-like component in knot B has properties inconsistent with an environment of pure stellar photoionization. It has a broad companion component with similarly high $O \text{ III} / H\beta$ and a velocity gradient of $\sim 200 \text{ km s}^{-1}$ over a barely resolved distance. We argue that shocks or stellar mass X-ray binaries are unlikely explanations, and conjecture that a weakly accreting intermediate mass or supermassive black hole is a more likely possibility. We sketch a heuristic model of how ejecta from such an accreting BH could be driving the expansion in the conspicuous ring feature North of the cluster.
8. We find that Haro 11 C, behind the outflowing gas system, has largely static gas to the North and in the center, then quite abruptly shows strong velocity variation although still no large scale ordered gas motion. The velocity field drops off to effectively zero, relative to the Star cluster, at the Southern end of the slit. To the North, the flux drops off steeply after first showing signs of being shocked. We interpret this as an outflow cone oriented perpendicular to the LOS, which collides

with dense, cold gas. A similar outflow cone we believe to be pointing south, with the strong and disordered motion being the result of a less dense and clumpier medium.

9. Knot C has a single component which is also not consistent with pure stellar photoionization by the BPT classification. It has been suggested that this cluster, too, may contain an accreting black hole, but while our observations seem consistent with this, they seem equally consistent with other explanations like e.g. shocks from strong supernova activity, and provide us no basis for favoring one explanation over the other.

7. ACKNOWLEDGMENTS

The Authors want to thank Claudia Scarlata, Ivana Orlitová and Beatriz Villarroel for insightful feedback and suggestions, and Lise Christensen for sharing her detailed knowledge about the X-Shooter. M.H. acknowledges the support of the Swedish Research Council, Vetenskapsrådet, and the Swedish National Space Board (SNSB) and is Academy Fellow of the Knut and Alice Wallenberg Foundation. G.Ö. is a Royal Swedish Academy of Science research fellow (supported by a grant from the Knut & Alice Wallenbergs foundation). This project has made extensive use of the Python-based packages Numpy (Walt et al. 2011), SciPy (Jones et al. 2001–), Matplotlib (Hunter 2007), Pandas (McKinney 2010), Astropy (Astropy Collaboration et al. 2013), LMfit (Newville et al. 2014), Sherpa (Doe et al. 2007), Statsmodels (Seabold & Perktold 2010), PyNeb (Luridiana et al. 2015), the R project for Statistical computing (R Core Team 2015), and others.

REFERENCES

- Adamo, A., Östlin, G., Zackrisson, E., et al. 2010, *MNRAS*, 407, 870
- Astropy Collaboration, Robitaille, T. P., Tollerud, E. J., et al. 2013, *A&A*, 558, A33
- Atek, H., Kunth, D., Hayes, M., Östlin, G., & Mas-Hesse, J. M. 2008, *A&A*, 488, 491
- Baldwin, J. A., Phillips, M. M., & Terlevich, R. 1981, *PASP*, 93, 5
- Basu-Zych, A. R., Lehmer, B., Fragos, T., et al. 2016, *ApJ*, 818, 140
- Bergvall, N., Marquart, T., Way, M. J., et al. 2016, *A&A*, 587, A72
- Bergvall, N., & Östlin, G. 2002, *A&A*, 390, 891
- Bergvall, N., Zackrisson, E., Andersson, B.-G., et al. 2006, *A&A*, 448, 513
- Bik, A., Östlin, G., Hayes, M., et al. 2015, *A&A*, 576, L13
- Calzetti, D., Armus, L., Bohlin, R. C., et al. 2000, *ApJ*, 533, 682
- Cannon, J. M., Skillman, E. D., Kunth, D., et al. 2004, *ApJ*, 608, 768
- Cardamone, C., Schawinski, K., Sarzi, M., et al. 2009, *MNRAS*, 399, 1191
- Cardelli, J. A., Clayton, G. C., & Mathis, J. S. 1989, *ApJ*, 345, 245
- Cleveland, W. S. 1979, *Journal of the American statistical association*, 74, 829
- Combes, F. 2005, in *American Institute of Physics Conference Series*, Vol. 783, *The Evolution of Starbursts*, ed. S. Hüttmeister, E. Manthey, D. Bomans, & K. Weis, 43–49
- Cumming, R. J., Fathi, K., Östlin, G., et al. 2008, *A&A*, 479, 725
- Doe, S., Nguyen, D., Stawarz, C., et al. 2007, in *Astronomical Society of the Pacific Conference Series*, Vol. 376, *Astronomical Data Analysis Software and Systems XVI*, ed. R. A. Shaw, F. Hill, & D. J. Bell, 543
- Duval, F., Östlin, G., Hayes, M., et al. 2016, *A&A*, 587, A77
- Ellison, S. L., Patton, D. R., Mendel, J. T., & Scudder, J. M. 2011, *MNRAS*, 418, 2043
- González Delgado, R. M., Leitherer, C., & Heckman, T. M. 1999, *ApJS*, 125, 489
- Grimes, J. P., Heckman, T., Strickland, D., et al. 2007, *ApJ*, 668, 891
- Gullikson, K. 2016, gullikson-scripts: Initial pre-release, , , doi:10.5281/zenodo.46604
- Guseva, N. G., Izotov, Y. I., Fricke, K. J., & Henkel, C. 2012, *A&A*, 541, A115
- Hanuschik, R. W. 2003, *A&A*, 407, 1157
- Hayes, M., Östlin, G., Atek, H., et al. 2007, *MNRAS*, 382, 1465
- Hayes, M., Östlin, G., Mas-Hesse, J. M., & Kunth, D. 2009, *AJ*, 138, 911
- Hayes, M., Östlin, G., Mas-Hesse, J. M., et al. 2005, *A&A*, 438, 71
- Hayes, M., Östlin, G., Duval, F., et al. 2014, *ApJ*, 782, 6
- Heckman, T. M., Hoopes, C. G., Seibert, M., et al. 2005, *ApJL*, 619, L35
- Herenz, E. C., Gruyters, P., Orlitova, I., et al. 2016, *A&A*, 587, A78
- Hoopes, C. G., Heckman, T. M., Salim, S., et al. 2007, *ApJS*, 173, 441
- Hunter, J. 2007, *Computing in Science Engineering*, 9, 90
- James, B. L., Tsamis, Y. G., Walsh, J. R., Barlow, M. J., & Westmoquette, M. S. 2013, *MNRAS*, 430, 2097
- Jia, J., Ptak, A., Heckman, T. M., et al. 2011, *ApJ*, 731, 55
- Jones, E., Oliphant, T., Peterson, P., et al. 2001–, *SciPy: Open source scientific tools for Python*, , [Online; accessed 2014-11-25]
- Kauffmann, G., Heckman, T. M., Tremonti, C., et al. 2003, *MNRAS*, 346, 1055
- Kennicutt, Jr., R. C. 1998, *ARA&A*, 36, 189
- Kewley, L. J., Dopita, M. A., Sutherland, R. S., Heisler, C. A., & Trevena, J. 2001, *ApJ*, 556, 121
- Kewley, L. J., Groves, B., Kauffmann, G., & Heckman, T. 2006, *MNRAS*, 372, 961
- Kramida, A., Yu. Ralchenko, Reader, J., & and NIST ASD Team. 2013, *NIST Atomic Spectra Database (ver. 5.1)*, [Online]. Available: <http://physics.nist.gov/asd> [2014, March 24]. National Institute of Standards and Technology, Gaithersburg, MD., ,
- Kunth, D., Leitherer, C., Mas-Hesse, J. M., Östlin, G., & Petrosian, A. 2003, *ApJ*, 597, 263
- Kunth, D., Mas-Hesse, J. M., Terlevich, E., et al. 1998, *Astronomy and Astrophysics*, 20, 11

- Leitet, E., Bergvall, N., Hayes, M., Linné, S., & Zackrisson, E. 2013, *A&A*, 553, A106
- Leitet, E., Bergvall, N., Piskunov, N., & Andersson, B.-G. 2011, *A&A*, 532, A107
- Luridiana, V., Morisset, C., & Shaw, R. A. 2015, *A&A*, 573, A42
- Marino, R. A., Rosales-Ortega, F. F., Sánchez, S. F., et al. 2013, *A&A*, 559, A114
- McKinney, W. 2010, in *Proceedings of the 9th Python in Science Conference*, ed. S. van der Walt & J. Millman, 51 – 56
- Micheva, G., Zackrisson, E., Östlin, G., Bergvall, N., & Pursimo, T. 2010, *MNRAS*, 405, 1203
- Newville, M., Stensitzki, T., Allen, D. B., & Ingargiola, A. 2014, *LMFIT: Non-Linear Least-Square Minimization and Curve-Fitting for Python*, , doi:10.5281/zenodo.11813
- Osterbrock, D. E., & Ferland, G. J. 2006, *Astrophysics of gaseous nebulae and active galactic nuclei*
- Östlin, G., Amram, P., Bergvall, N., et al. 2001, *A&A*, 374, 800
- Östlin, G., Amram, P., Masegosa, J., Bergvall, N., & Boulesteix, J. 1999, *A&AS*, 137, 419
- Östlin, G., Cumming, R. J., & Bergvall, N. 2007, *A&A*, 461, 471
- Östlin, G., Hayes, M., Kunth, D., et al. 2009, *AJ*, 138, 923
- Östlin, G., Marquart, T., Cumming, R. J., et al. 2015, *A&A*, 583, A55
- Östlin, G., Hayes, M., Duval, F., et al. 2014, *ApJ*
- Overzier, R. A., Heckman, T. M., Kauffmann, G., et al. 2008, *ApJ*, 677, 37
- Overzier, R. A., Heckman, T. M., Tremonti, C., et al. 2009, *ApJ*, 706, 203
- Prestwich, A. H., Jackson, F., Kaaret, P., et al. 2015, *ApJ*, 812, 166
- R Core Team. 2015, *R: A Language and Environment for Statistical Computing*, R Foundation for Statistical Computing, Vienna, Austria
- Rivera-Thorsen, T. E., Hayes, M., Östlin, G., et al. 2015, *ApJ*, 805, 14
- Sandberg, A., Östlin, G., Hayes, M., et al. 2013, *A&A*, 552, A95
- Schlegel, D. J., Finkbeiner, D. P., & Davis, M. 1998, *ApJ*, 500, 525
- Seabold, J., & Perktold, J. 2010, in *Proceedings of the 9th Python in Science Conference*
- Vader, J. P., Frogel, J. A., Terndrup, D. M., & Heisler, C. A. 1993, *AJ*, 106, 1743
- Verhamme, A., Orlitová, I., Schaerer, D., & Hayes, M. 2015, *A&A*, 578, A7
- Vernet, J., Dekker, H., D’Odorico, S., et al. 2011, *A&A*, 536, A105
- Walt, S. v. d., Colbert, S. C., & Varoquaux, G. 2011, *Computing in Science & Engineering*, 13, 22
- Wofford, A., Leitherer, C., & Salzer, J. 2013, *ApJ*, 765, 118
- Östlin, G., Bergvall, N., & Roennback, J. 1998, *A&A*, 335, 85

APPENDIX

A. RECTIFICATION PROCEDURE FOR 2D SPECTRA

To compensate for the slit direction drift in continuum trace and ensure a one-to-one correspondence between slit-direction pixel coordinate and physical position, we rectified the 2D spectra by the following procedure.

We fitted each column in the 2D spectrum to a single Gaussian profile, and interpreted the center of this as the center of the continuum trace in said column. From a histogram of these values, ignoring columns around known extended emission features, values deviating by more than σ from the mean were rejected. The remaining centroid distribution was then fitted by a Local Linear Estimator (LLE) using the `KernelReg` class from the Python package `statsmodels.nonparametric.kernel_regression`, with kernel width selected by least-squares cross validation. Each column was then shifted vertically by linear interpolation by the distance between its LLE-fitted centroid and the reference value, chosen to be the centroid value around $H\alpha$, using the `ErrorPropagationSpline` Python class (Gullikson 2016), which propagates errors by Monte Carlo sampling. The process was repeated for the VIS arm to improve outlier rejection. The resulting 2D spectra have a fixed correspondence between lengthwise slit- and physical position.

As an example, figure A1 shows the 2D VIS spectrum of Haro 11 B before (upper panel) and after (lower panel) being rectified. In the upper panel, the column centroids (orange dots) remaining after line and outlier rejection, and the LLE (solid green), are superimposed on the observed data. The misalignment in the upper panel is visible to the naked eye, with an offset between the blue and the red end of ~ 3 pixels $\approx 0.5''$, or about half the reported seeing.

B. FIT QUALITY AND CONFIDENCE ESTIMATES

B.1. Residual maps

Residuals from modeling are shown in figures B2, B3, and B4 for ESO 338, Haro 11 B and Haro 11 C, respectively. Color shows excess emission as orange, excess absorption as black, with zero is shown as white. Noisy regions are largely background, white regions are well fitted regions divided by large flux. The presence of dark or orange features indicates where there is poorer agreement between model and data. Nearby, unmodeled lines are visible in orange in some panels, e.g. a couple of high-order Balmer lines around the [O II] doublet in ESO 338, or [N II] 6548 immediately bluewards of $H\alpha$. We caution the reader that comparatively small discrepancies in line wings, bordering noisy regions, appear as strong as much stronger features in the white regions of strong flux. Thus, the darker shade bluewards of line center in the upper ~ 15 rows of $H\alpha$ in Haro 11 B hold only a fraction of the flux of e.g. the faint black-white-blue feature ~ 200 km on the red side of line center between rows 40 and 60 in the [O III] 5007 feature of the same system - a signature of misalignment of model and data peak centroids. Furthermore, particularly in the UVB arm, a number

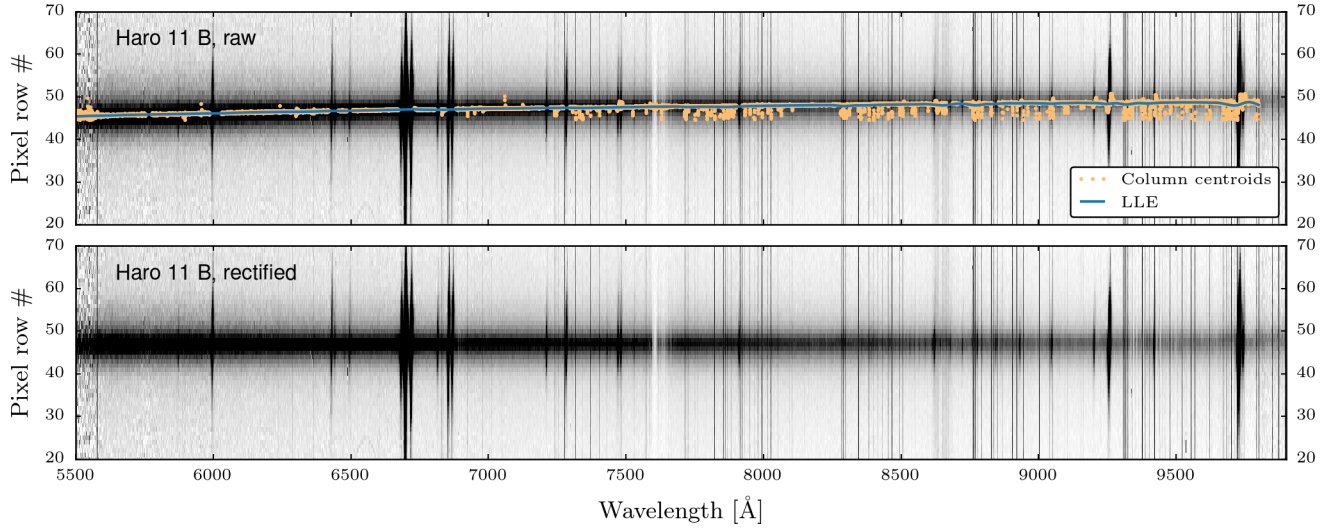


Figure A1. 2D VIS spectrum of Haro 11 B, with fitted centroids (orange dots) and the local linear estimator of the continuum trace (blue curve) overplotted. The procedure was repeated for the VIS arm, with outlier rejection being more efficient the second time. Pixels are strongly elongated in the vertical direction. The $H\alpha$ + [N II] triplet is clearly visible around $\lambda = 6700$, and the [S II] $\lambda\lambda 6717, 6731$ doublet to its right.

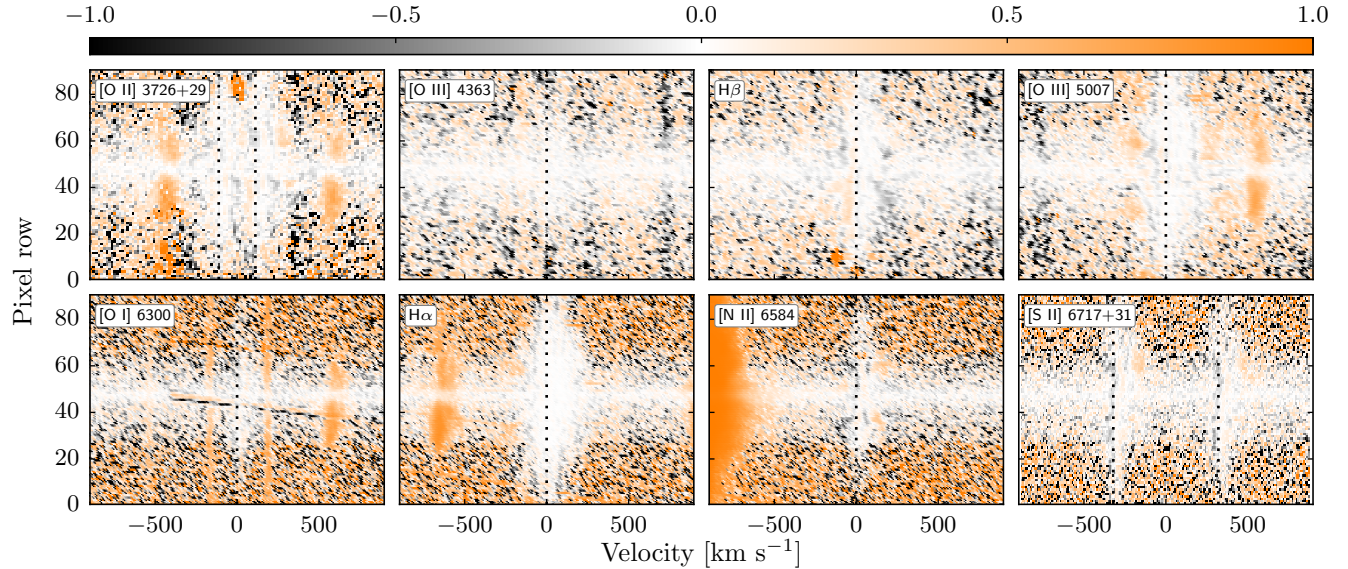


Figure B2. Residuals from subtraction of model from data for ESO 338. All lines have been modeled using $H\alpha$ as a template for component positions and widths; see sect. 3 for details. Note the difference in agreement between lines in the UVB arm (up till and including [O III] λ 5007) and the VIS arm.

of narrow, vertical absorption features are visible.

In ESO 338, there is a faint but broad feature of excess emission bluewards and excess absorption redwards of line center just below the continuum, suggesting a slight misalignment of a broad but not very luminous component. In $H\alpha$, vertical streaks of slight residual absorption suggests that the profile in general is dropping off faster than the model in the wings, probably a result of a somewhat oversimplified model. Residual emission from the spike structure of [N II] 6583 is visible in the residuals, as is a morphologically similar feature in absorption on the opposite side of line center in the same slit region. This second component looks similar to the emission feature in strength, but the absolute flux there is lower (see fig. 3) and thus the feature in actuality less important.

In Haro 11 B and C, the far sides of the [N II] 6548+83 doublet from $H\alpha$ are visible as sharply cutoff black regions. The line ratio of same doublet is also reflected in the higher noise levels on the red side of $H\alpha$ and the blue side of [N

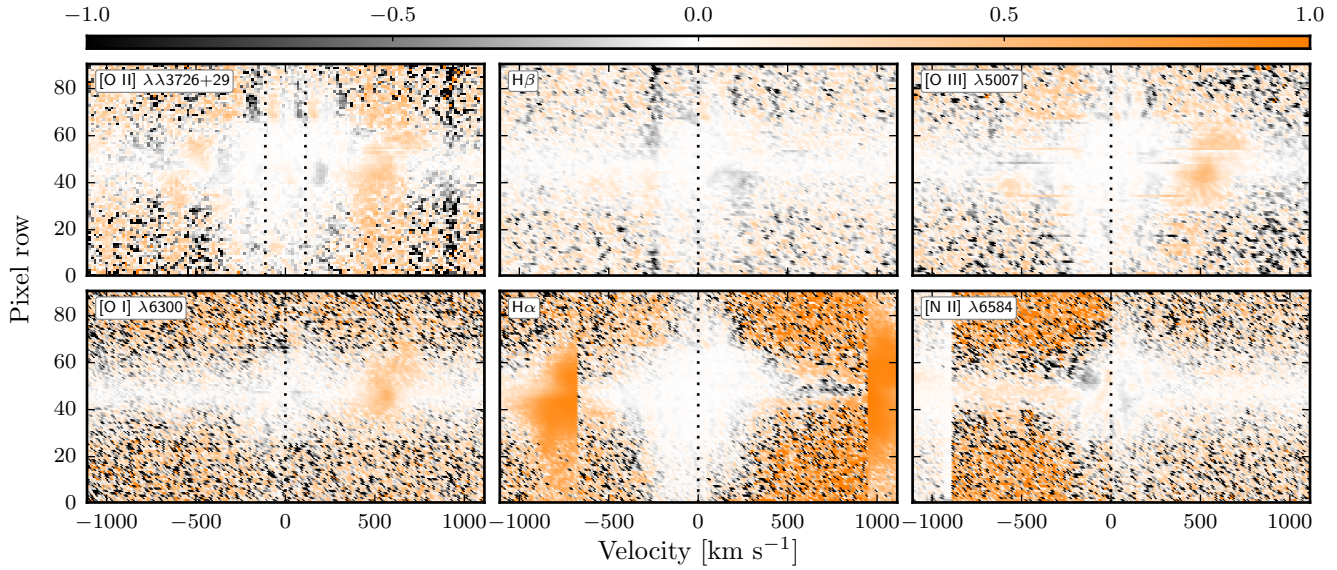


Figure B3. Same as figure B2; but for Haro 11 B. The line at λ 4363 of [O III] and the [S II] λ 6717+31 doublet are not included for either of the Haro 11 spectra.

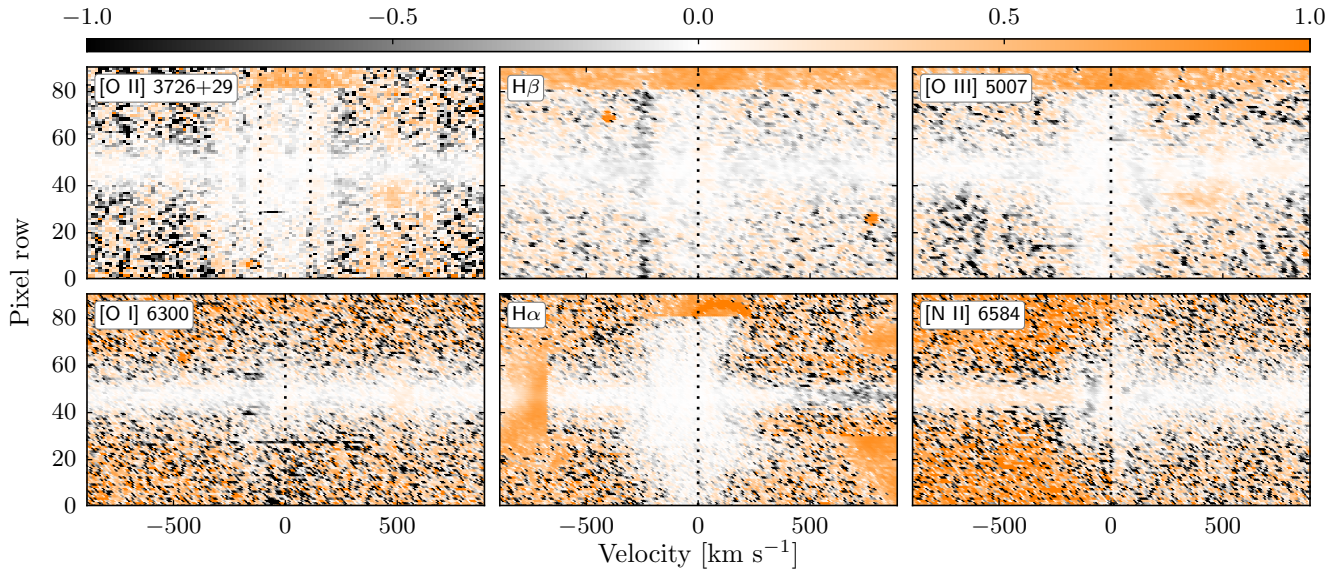


Figure B4. Same as figure B2; but for Haro 11 C.

II] 6583 in these systems. Next to [O III] 5007, emission from the He I 5016 feature is visible; due to the line width in this system, this feature is blended with [O III] 5007 and a likely contributor to the poorer fit in some of the pixel rows, visible as dark or orange horizontal streaks in the line wings. This is only likely to have affected faint, broad components. In several of the lines, most notably [O II] 3726+29, but also in [O III] 5007, H β and even H α , a vertical tricolor-pattern is seen in the rows $\sim 70 - 80$, again a telltale sign of an offset peak centroid. In this region, as can be seen in fig. 9, the line is modelled by 1 or 2 components, and has a tall peak which is somewhat skewed, similar to what is seen (less conspicuously) in component *f* in fig.8. The continuum trace in H α ([N II] 6583) shows slight over (under) subtraction in the red (blue) wing, revealing that a broad but faint component of H α may in fact blend beyond the line center of [N II] 6548, resulting in a slight overestimate of this line's flux in this region, and a corresponding underestimate of the red wing of H α in the same rows.

In Haro 11 C, the upper 10 rows have not been modelled and thus appear darker than the rest. In addition, many of the comments about Haro 11 B also apply here, including the slight spillover of H α into the blue side of [N II] 6548, and blending of He I 5016 with [O III] 5007. [N II] 6548+83 only blends with H α in the central region and thus, to

preserve SNR, no subtraction has been performed in rows < 30 and > 65 .

B.2. Uncertainty estimates

To approximate the deterministic component of parameter variation, we performed a Robust Locally-Weighted Regression, or LOESS. The basic procedure for this technique is described (under the name LOWESS) by Cleveland (1979). To summarize the procedure: For each point x_i in the independent variable, it fits the measured variable in a window around x_i to an n th degree (in most cases, $n = 1$) polynomial, with the data weighted by a kernel $w_i(x_i)$ around x_i . Here the standard tricubic kernel was used. The value of the fit polynomial in x_i , \hat{y}_i (generally $\hat{y}_i \neq y_i$), is adopted as the fit value in this point, and the procedure is repeated for all points. For robustness to outliers, the data are then re-weighted from the scale of the residuals, such that points with poor agreement with the initial fit are weighted less and points with better agreement weigh more. For the residuals of the initial regression, a set of weights δ_i is computed for each x_i from a bisquare function (still from Cleveland 1979):

$$\begin{aligned} B(x) &= (1 - x^2)^2 && \text{for } |x| < 1 \\ &= 0 && \text{for } |x| \geq 1 \end{aligned} \tag{B1}$$

For the residuals $e_i = y_i - \hat{y}_i$, and with s being the median of the $|e_i|$, the weights are computed as

$$\delta_k = B(e_k/6s) \tag{B2}$$

These weights are then combined with the original weighting kernel, and the linear regression step is repeated with the combined weights $\delta_i w_i(x_i)$. The full process is then iterated a number of times (mostly, 2-3 iterations is sufficient for convergence). The remaining, bisquare-weighted residuals are then expected to be randomly drawn from a distribution around 0 representing the noise in the given parameter. The implementation used here is the function `loess` in R which is a generalization of Cleveland's LOWESS procedure that allows for assigning individual weights to data points to combine with the weights inherent to the procedure, letting us compute the confidence intervals on flux-weighted data just as the computed averages are.

This method has a few advantages: where it is possible, the directly measured scatter in a parameter is a better measure of its uncertainty than propagated uncertainties, as it implies fewer assumptions of symmetric, normal distributed and independent uncertainties. Especially, it is useful for deriving an uncertainty of the mean in the case where the noise distribution is long-tailed, like e.g. Cauchy (Lorentz) distributed. When tested on a sine function with noise and frequency and phase perturbations drawn from a Cauchy distribution, the true data mean fell within the value errorbars of the value recovered from 20 data points 85% of the time, somewhere in between the typical 67% and 95% confidence levels typically reported. However, one should also keep in mind that some of the components contain only a few data points. This can lead to the LOESS regression overfitting the available data and underestimating the noise component. We have attempted to minimize this effect by forcing a minimum kernel width on the loess function. Small numbers also enlarge uncertainties in the inferred statistical distribution of the noise and by extension the reported errorbars. Finally, and related to this, small numbers can make it more difficult to assess whether the errors are symmetric in a parameter. Since errors are symmetric in line fluxes, one would not expect them to also be symmetric in e.g. $E(B - V)$, but visually they appear to be.

Still, despite these caveats, we believe that the errors reported here are a more accurate measure of uncertainties than the ones obtained by propagating error estimates from the individual line fits.